7

Magnetic Switching in High-Density MRAM

J. Shi

The anticipated commercialization of magnetoresistive random access memory (MRAM) chips spurs a great deal of interest in the magnetism community. Since non-volatile information is stored on increasingly shrinking magnetic elements in high-density MRAM, magnetic switching of patterned nanostructure elements plays a key role in memory functioning. In this chapter, we will first briefly review the existing mainstream semiconductor memories, followed by a review of different modes of MRAM. Then we will concentrate on magnetic switching and the effect of switching on selectivity for reading and writing in structures ranging from ideal single domains to patterned thin film elements whose dimensions are much greater than single domain. Lastly, we will discuss some specific issues related to magnetic switching in increasingly high-density MRAM.

7.1 Random Access Memories (RAMs)

Built in the 1950s, the earliest memory storage device for commercial computers was the "ferrite-core memory", which consists of wire wound doughnut-shaped coils [7.1, 2]. Since it was slow ($\sim$1 ms access time), bulky ($\sim$1 mm per bit) and expensive ($\sim$1 cent per bit), it was rendered obsolete by semiconductor memories in the 1970's. RAMs are referred to as solid state memory devices that do not use any moving parts. Due to the great advances in semiconductor technology in the last three decades, today's RAMs are being built with ever-increasing memory performance while dramatically reducing cost [7.3]. The basic unit of a RAM device is the memory cell. Multiple rows and columns of cells are arranged to form a large two-dimensional (2D) array that can be accessed quickly and directly, which is different from serial access memory devices such as shift registers or recording tapes. According to the memory cell functions, there are several different types of semiconductor RAMs [7.4], ranging from the most commonly used ones such as static-RAM (SRAM), dynamic-RAM (DRAM), and Flash (a type of electrically erasable programmable read only
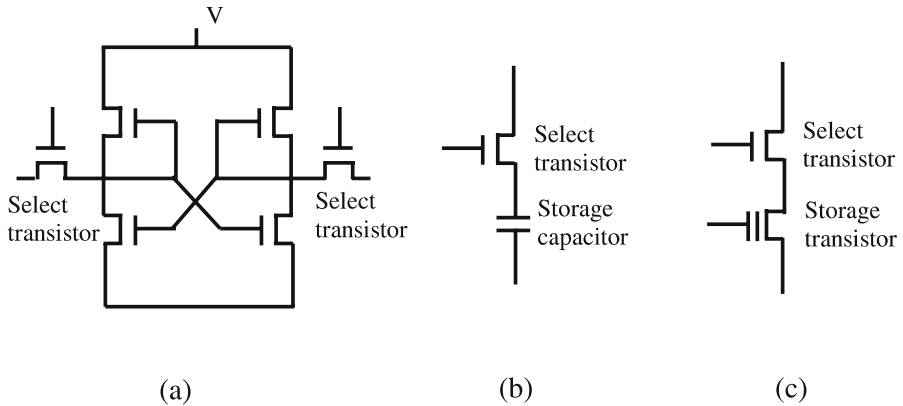
Fig. 7.1. Memory cell architecture for three types of RAMs. (**a**) SRAM. (**b**) DRAM. (**c**) EPROM/EEPROM (EPROM stands for erasable programmable read only memory)

memory or EEPROM), to ferroelectric-RAMs (FeRAM or FRAM). In this section, we briefly review those commercially available RAMs.

SRAM is generally used for cache memory in computers. Its cell consists of a basic flip-flop circuit that needs a DC current to retain its memory [7.3, 4]. Each cell contains four transistors plus two additional transistors (shown in Fig. 7.1a) or two load resistors as pull-up devices. Either diagonal transistor pair can be simultaneously on or off, representing two stable memory states. The gate electrodes of the horizontal memory cells are linked to form rows and the sources or drains of the vertical cells are linked to form columns. When a particular cell in the 2D array is selected for writing, a voltage pulse applied to one select transistor of the cell allows the cell to store a "0", or the other select transistor to store a "1". For reading, the asymmetry of the current flow in the select transistors distinguishes the state "0" from the state "1". SRAM is a very fast memory, but it requires a relatively large cell area and it is relatively more expensive to build. The memory state disappears when power is turned off; therefore, it is a volatile memory.

A DRAM cell consists of one select transistor and a storage capacitor (Fig. 7.1b) [7.3, 4]. Hence, DRAM is simpler and denser than SRAM. A charged capacitor represents a "1"; a discharged capacitor represents a "0". When a cell is selected for reading, the electrons stored in the capacitor flow to the column wire, changing the memory state to a "0" and the resulting current pulse is picked up by a sense amplifier. This pulse is interpreted as a "1", but meanwhile, the original "1" state is destroyed. This reading process is called destructive readout (DRO). Each time such a cell is read, the "1" needs to be rewritten. In addition, the charge stored in the storage capacitor cannot be held there indefinitely due to leakage; therefore, the DRAM cells need to be refreshed every millisecond or so. As a result, DRAM is not as fast as SRAM, and it is also a volatile memory.

The one transistor plus one ferroelectric capacitor (1T/1C) FRAM cell architecture [7.5] is similar to that of the DRAM cell, except that the capacitor is replaced

by a ferroelectric capacitor which can permanently hold the charge. Furthermore, the polarity of the capacitor can be switched by a voltage; therefore, the two polarization states serve naturally as two stable memory states. $PbZr_{1-x}Ti_xO_3$ (PZT) is an example of the ferroelectric material used for these capacitors. FRAM is a non-volatile memory, but it has limited read/write endurance ($< 10^{13}$ cycles).

Figure 7.1c shows an EPROM/EEPROM cell [7.3, 4]. The storage transistor has two gates: a control gate and a floating gate separated from the control gate by a layer of silicon dioxide. The floating gate is used for storing charges, which represent the memory states. When a cell is selected for writing, a high applied drain voltage causes electrons to transfer to the floating gate. The electrons pass through the oxide layer to the floating gate by "hot" injection or avalanche injection in the case of EPROM, and by Fowler-Nordheim tunneling mechanism in EEPROM. The tunneling requires a thin oxide layer ($< 10\,nm$ in thickness). Another difference between the EPROM and EEPROM is in the erasure. In EPROM, cells are erased by shining ultraviolet light on the whole memory chip. Electrons at the floating gate gain enough energy to jump the energy barrier of the oxide. In EEPROM, electrons can leave the floating gate by Fowler-Nordheim tunneling in a reversed voltage. In state "1", electrons at the floating gate shift the threshold of the transistor; therefore, it can be read out from the current. Flash memory is one type of EEPROM. It is a high-density and non-volatile memory. However, it has limited write endurance (10^5–10^6 cycles). It requires high voltage (5–12 V) and has slow programming (ms) and erase (sec) times.

7.2 Magnetoresistive Random Access Memory (MRAM)

In spite of tremendous advances made in the solid state RAMs in the past three decades, there has been no single commercially available solid state memory that possess all the desirable attributes: non-volatile, fast, dense, low power consumption, unlimited read/write endurance, yet economical. MRAM is a newly developed memory that possibly offers such potential [7.6]. Prototypes of MRAM have already been demonstrated by Motorola (Fig. 7.2), [7.7] IBM, and Honeywell after only a few years of active research and development. Commercial MRAM chips of at least 1 megabit (1 Mb) are anticipated in year 2003-2004 [7.8].

The modern MRAM concept resembles the early magnetic ferrite-core memory. They both utilize bi-stable remanent magnetization states to store information; therefore, they are intrinsically non-volatile. Memory cells are row and column addressable and are written by the magnetic fields generated by two sets of current lines. The write access time is determined by the magnetic switching speed of the materials, which is inherently fast (~ 1 ns or less). The two memories differ in the way the memory bits are read. The ferrite-core memory uses an inductive method to sense the magnetization direction stored in the rings. When a particular cell is selected for reading, the orthogonal fields generated by the two lines interrogate the memory element. The inductive signal level depends on the original magnetization state with respect to the resultant field direction. In magnetoresistive RAMs, the magnetoresistance (MR) of a cell is used to directly discern the memory states. In general, the higher the MR
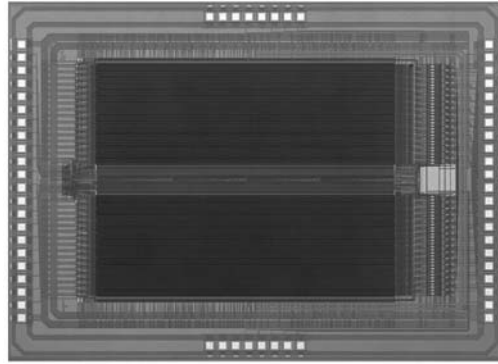
Fig. 7.2. 1 Mb MRAM chip demonstrated by Motorola in 2002. (Courtesy of Motorola Labs)

ratio the cell material has, the shorter the read access time. Recent breakthroughs in thin film magnetism marked by the discoveries of giant magnetoresistance (GMR) and tunneling magnetoresistance (TMR) provided an enormous impetus to MRAM research. There are several different types of MRAM designs according to the MR mechanism. In the following subsections, we will review a few variations of MRAM.

7.2.1 Anisotropic Magnetoresistance-based MRAM

Many ferromagnetic metals and alloys exhibit sizeable anisotropic magnetoresistance (AMR) [7.10]. The resistance of the materials not only changes with applied magnetic field strength, but also depends on the direction of the applied field, which determines the magnetization orientation. When the field is applied along the electrical current such that the magnetization is parallel to the current flow, the resistance is greater than when the field or the magnetization is perpendicular to the current flow. The AMR effect was explained by Kondo [7.11] in terms of the scattering of s-electrons by a small unquenched orbital moment induced by 3d spin moment. This effect can be as large as 4%.

Memory states: An AMR based-RAM cell is a narrow stripe consisting of two magnetic layers separated by a non-magnetic conducting layer, such as a three-layer stack of permalloy ($Ni_{81}Fe_{19}$)/ tantalum nitride (TaN)/ permalloy [7.12]. The permalloy films have an induced anisotropy during film deposition with the anisotropy axis set along the width of the etched stripe. When the isolated cells are electrically linked to form a column (or row), the line carries a "sense" current that is used to sense the memory state of a cell when it is selected. The sense current also generates a "sense field" that acts on the two magnetic layers in opposite directions according to the right-hand rule. Orthogonal isolated current lines, called "word lines", generate magnetic fields perpendicular to the anisotropy axis. The remanent magnetization state of the two permalloy layers can have either clockwise or counterclockwise configurations around the sense current, which serve as two stable memory states. In the absence of any magnetic field, these two states give rise to the exact same

Table 7.1. A summary of the main features of MRAM in comparison with other mainstream RAMs (Courtesy of the MRAM Development Alliance of IBM and Infineon Technologies) [7.9]

	SRAM	DRAM	NAND Flash	NOR Flash	1T1 MTJ MRAM	XPC MRAM
	Existing Products				Technology Products	
Cell size in F^2	100	8	5	6	> 8 [published 20–40]	> 4
Supply Voltage	2.5 V	2.5 V	1.8 V	3.3 V	1.8 V [pusblished 2.5–3.3 V]	1.8 V
Retention Power	1 µW –375 mW	10 mW	0	0	0	0
Retention Time	∝ [with power]	64 ms	10 yrs	10 yrs	10 yrs	10 yrs
Random Read Access	2–100 ns	60 ns	10 µs	90 ns	10–50 ns [published 3–50 ns]	50 ns–11 µs
Random Write	2–100 ns	60 ns	100 µs [erase 100 ms]	10 µs [erase 100 ms]	10–40 ns [published 3–50 ns]	20–40 ns
Endurance	> 10^{15}	> 10^{15}	> 10^{15} read 10^{15} write	> 10^{15} read 10^{15} write	10^{15} [expected]	10^{15} [expected]

resistance, because the layer magnetization in both states is perpendicular to the sense current direction.

Reading: Let's consider state "0" and state "1" as shown in Fig. 7.3. When a pair of sense and word currents is simultaneously turned on, only the memory cell at the crossing of the current lines experiences two magnetic fields. Memory states "0" and "1" respond to the fields differently, resulting in different MR. This produces different signal levels in the sense line. Fig. 7.4 is a top view of the two layer magnetization configurations for both memory states when a sense and word field is applied for reading. The sense current flowing through the memory cell creates a clockwise or counterclockwise field. The word current creates a word field along the length of the memory cell. For a fixed sense current direction as shown in Fig. 7.3, the combination of the sense and word currents turns the layer magnetization in state "0" towards the direction of the sense current flow, therefore increasing the resistance of the cell due to AMR. However, the same combination of the sense and word fields has a much smaller effect on the magnetization in state "1". Therefore, compared with the resistance in the remanent state, the resistance rise of state "1" is much smaller

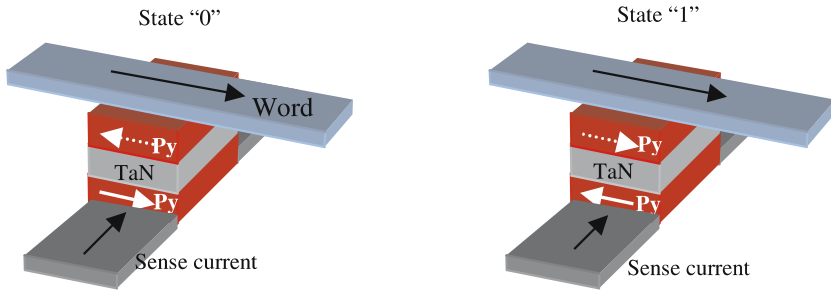State "0"   State "1"

Fig. 7.3. Two memory states in an AMR-based memory cell. The easy axs direction of the two permalloy (Py) layers is set along the width of the etched stripe. The word line is electrically isolated with the memory cell
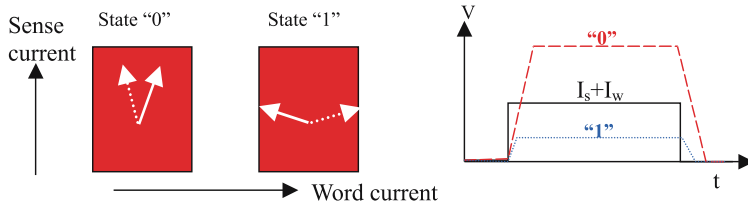

Fig. 7.4. Read operation in AMR memory cells. Magnetization configurations for two memory states during reading. The *dashed line* represents the top layer magnetization and the *solid line* the bottom layer magnetization (left). The sense signal form state "0" and state "1" for a current pulse $I_s + I_w$ (right)

than that of state "0". In the reading operation, the resultant field from the sense and word currents must be kept below the switching threshold so that the magnetization rotation is reversible. Hence, the original state is preserved after the reading is done. This is the non-destructive readout (NDRO) scheme.

It should be pointed out that when a pair of sense and word currents is turned on, the other memory cells along either the sense or word line also experience a field. These cells are called "half-selected" cells. For the half-selected cells along the sense line, the magnetization does not change regardless of their memory state. For the half-selected cells along the word line, the magnetization does rotate away from the easy-axis direction, but because they are not on the sense line, their resistance change does not contribute to the sense signal. After the word current is turned off, these cells restore to their remanent states. In real AMR-based RAM devices, because of edge effects, the maximum differential resistance of a cell between a "1" and a "0" is only about 1/4 of the total AMR, or about 0.5%. The sense signal is very small; therefore, the read access speed is slow. In 16 Kb integrated MRAM chips, the read access time is about 250 ns [7.13].

Writing: State "0" can be written into state "1" and vice versa by increasing the current flow in both the sense and word lines. When the resultant field strength

exceeds the switching threshold, states "0" and "1" can be switched to each other. The magnitude of either current is chosen such that a single field is not strong enough to switch the magnetization. In all MRAM devices, the cell selection for writing is accomplished by this half-select scheme, which will be discussed in more detail in following sections.

AMR-based RAMs for the first time demonstrated the possibility of solid state memory devices using MR for readout. But it has a relatively long read access time. The memory mode described here apparently stops working for submicron and smaller memory cells because the shape anisotropy dominates thus the memory states are different. To improve the read access time, a large signal, i.e. a large MR is required.

7.2.2 Spin-Valve MRAM

The discovery of the giant magnetoresistance (GMR) effect [7.14, 15] was a turning point in MRAM research and development. GMR originates from the spin-dependent scattering in alternating ferromagnetic/non-magnetic multilayers. The multilayer resistance depends on the relative orientation of magnetization in adjacent layers. In low field applications such as read heads, the original antiferromagnetically coupled multilayers are not used, primarily due to the strong interlayer exchange coupling (∼1 kOe). A simpler and more practical structure is the spin-valve (SV). A SV structure consists of only two magnetic layers separated by a thin conducting spacer layer (e.g. 3 nm thick Cu layer). One of the two magnetic layers is magnetically pinned by an antiferromagnetic material (e.g. FeMn or IrMn) due to exchange anisotropy, and the other layer is free to rotate under a relatively small magnetic field. If the applied magnetic field strength is greater than the coercive field of the unpinned magnetic layer (or free layer) but smaller than the exchange pinning field, the free layer magnetization is switched parallel or anti-parallel to the pinned layer magnetization. In consequence, a large change in resistance (GMR) is realized between the two states. The change in resistance is typically about 5%, but in optimized films it can be as high as 17% [7.16].

Memory states: The memory states of a SV MRAM cell are the two remanent magnetization states of the free layer (Fig. 7.5). The pinned layer magnetization does not change; therefore, it only serves as a reference for the free layer.

Reading: In a one-transistor-per-cell architecture [7.17], the transistor is used for selecting the cell as well as sensing the in-plane resistance of the cell when selected. The cell selection for reading is achieved by turning on a select transistor whose gate and source (or drain) are connected to a row (bit line) and a column (word line) respectively. When a pair of row and column lines is chosen, the cell at the crossing is selected, and the remanent state resistance of the cell is read and compared with a reference cell. The memory state is determined by the sense voltage signal. Since the magnetization state is not disturbed during reading, the reading operation is non-destructive.

Writing: The one-transistor-per-cell design requires another set of lines called digit lines parallel to the word lines for writing operation. The digit line provides an

orthogonal field to the field generated by the sense current. A pair of sense and digit current lines is simultaneously turned on to select the cell at the crossing for writing, similar to the half-select scheme in AMR-based RAM.

7.2.3 Pseudo-Spin-Valve (PSV) MRAM

A second type of GMR-based memory is PSV MRAM. PSV memory cells are similar to SV cells, except that both layers of a PSV cell are switchable but they switch at different fields. The two magnetic layers can be made of different materials or the same material with different film thickness. In the latter case, the coercive field becomes dependent upon the film thickness when the lateral dimensions are below 1 μm [7.18]. Here we focus on the latter PSV cells.

Memory states: When a PSV film is patterned to submicron stripes, the magnetization of each layer is along the cell length at the remanent state due to shape anisotropy. There are in principle four possible memory states in a PSV memory cell, e.g. two parallel and two anti-parallel states. In actual PSV MRAM, only two magnetization states of the thicker layer are used to store information [7.19, 20], as shown in Fig. 7.6. Similar to the two states in an AMR cell, memory states in a PSV cell have the same remanent resistance; therefore, they cannot be distinguished by simply sensing their static resistance.

Reading: The thin magnetic layer in a PSV cell is used for reading. When a sense line is turned on, the sense current flows through all the cells along the line. However, if a perpendicular word line is turned on, only the cell at the crossing is selected. To read the selected cell, the resultant field from both the sense and word lines has to be strong enough to switch the thin layer magnetization, i.e. greater than H_{c1}, but less than the switching field of the thick layer, H_{c2}. In addition, the fields from either line must be small enough such that the thin layer magnetization of the half-selected cells along either line is not switched. The reading operation is executed in the following steps. First, a negative word field is applied so that the resultant field on the selected cell is between $-H_{c1}$ and $-H_{c2}$, which initializes the state of the
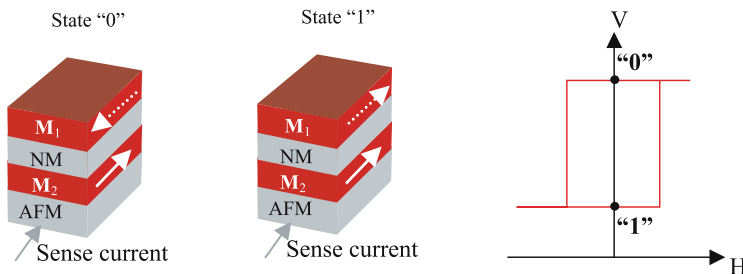

Fig. 7.5. Memory states "0" and "1" in a SV MRAM cell. The bottom layer magnetization is pinned and the magnetization direction of the top layer represents the memory state (left). The voltage is high or low depending on the memory state (right)
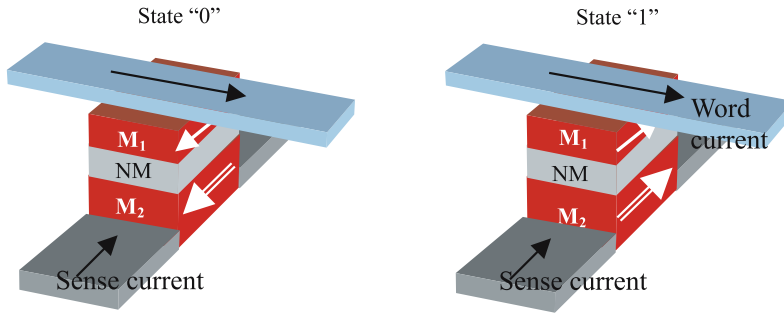
Fig. 7.6. Memory states in a PSV cell. A certain length-to-width aspect ratio is needed for obtaining large signal. The overall magnetization direction of both layers can be either parallel or anti-parallel to each other along the cell length. The etched PSV cells are electrically connected to form a sense line (vertical scale is out of proportion). The word lines are electrically isloated from the cell
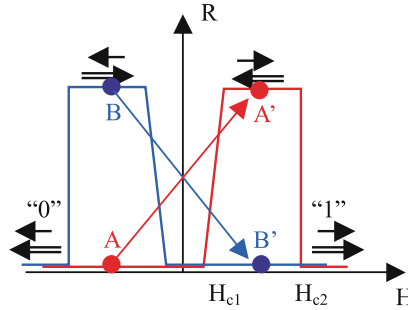

Fig. 7.7. Reading operation in PSV MRAM. The thin layer is interrogated by two sequential word pulses: a negative one to initialize the cell and followed by a positive one to check the voltage change. The combined field strength is set between H_{c1} and H_{c2}

thin layer. In doing so, state "0" is set to point A on the red curve, and state "1" to point B on the blue curve. Next the sense amplifier is auto-zeroed, and the word current pulse ramps to a positive field so that the resultant field is between $+H_{c1}$ and $+H_{c2}$. Hence, state "0" goes from A to A' and state "1" goes from B to B'. The cell voltage signal with respect to zero is negative for state "1" and positive for state "0". The difference in resistance swing between the two states is twice as much as the full MR of the materials. This is also called dynamic read-out scheme. To the half-selected cells along the sense line, the magnetization of both layers rotates away from the equilibrium position but neither would switch. As the sense field is set back to zero, the respective original states are restored. To the half-selected cells under the word current, the magnetization of neither layer changes; therefore, these cells are not disturbed.

Writing: To change from one memory state to the other, a higher field ($> H_{c2}$) is needed to switch the thick layer magnetization. In actual MRAM chips, the writing

may need another set of current lines called digit lines parallel to the sense lines to aid to the sense field. In addition, "wrap-around" word current lines are used to generate a higher and more uniform field [7.19].

In PSV MRAM, all the cells along a sense line share one transistor. It is a denser design than one-transistor-per-cell architecture in SV MRAM. Furthermore, the effective signal is doubled using dynamic read-out scheme; therefore, it is advantageous in terms of the read access speed. Nevertheless, there are serious drawbacks. First, in order to ensure a reasonable separation between H_{c1} and H_{c2}, a thick film is usually used for a high H_{c2}. Hence, writing demands a large current, which means large transistors. Second, similar to SV MRAM, PSV cells often need large aspect ratio to gain higher signal and faster read access speed. Large aspect-ratio cells occupy more area and also require higher switching fields, which compromises memory density as well as power consumption.

7.2.4 Magnetic Tunnel Junction (MTJ) MRAM

Clearly, a key to high-speed, high-density, and low power MRAM is the high signal level ΔV or large magnetoresistance ΔR, not necessarily the high MR ratio $\Delta R/R$. In all-metal GMR structures, the speed, density, and power consumption are often incompatible with each other. The magnetic tunnel junction (MTJ) material having large tunnel magnetoresistance (TMR) provides real potential for high performance MRAM [7.21]. So far it is the most attractive MRAM, and many companies are vigorously pursuing it. In fact, MTJ MRAM cells and prototype chips have demonstrated outstanding performance in terms of the access times, cell size, and power consumption. In this chapter, we will not go to details about the TMR effect and MTJ materials, which are reviewed by Moodera in separated chapters of volume III.

MTJ cell resistance and signal: MTJ materials consist of two ferromagnetic layers separated by a thin insulating layer (1–2 nm thick) such as Al_2O_3 [7.22–25]. Since the resistance of a MTJ junction is inversely proportional to the area of the junction cross-section, an appropriate quantity to describe the specific resistance is the product of the resistance and the area of the junction, or the *RA* product. The tunneling current flowing through the insulating layer depends exponentially on its layer thickness [7.26]. Hence, by controlling the thickness of the oxide layer the RA product can be tuned over many orders of magnitude. In general, it is relatively easy to control the oxide layer thickness when the layer is thick, but it is rather challenging to produce a very thin oxide layer for low RA product MTJ films.

The magnetoresistance ratio $\Delta R/R$ is on the other hand determined by the spin-polarization of the magnetic layers on both sides of the tunnel barrier [7.27]. Nowadays very large TMR ($\sim 50\%$) can be routinely achieved in sputtered MTJ films in several laboratories. Although the TMR ratio decreases with the increase of the voltage bias, the usable TMR at a reasonable bias ($\sim 200\,mV$) can be still significantly large compared with that of PSV materials ($> 20\%$) [7.28].

With the high resistance and TMR ratio, the signal level of a MTJ cell (ΔR or ΔV between the two memory states) is very favorable, which is essential to fast read access in MRAM. This also brings additional benefits such as high-density and low
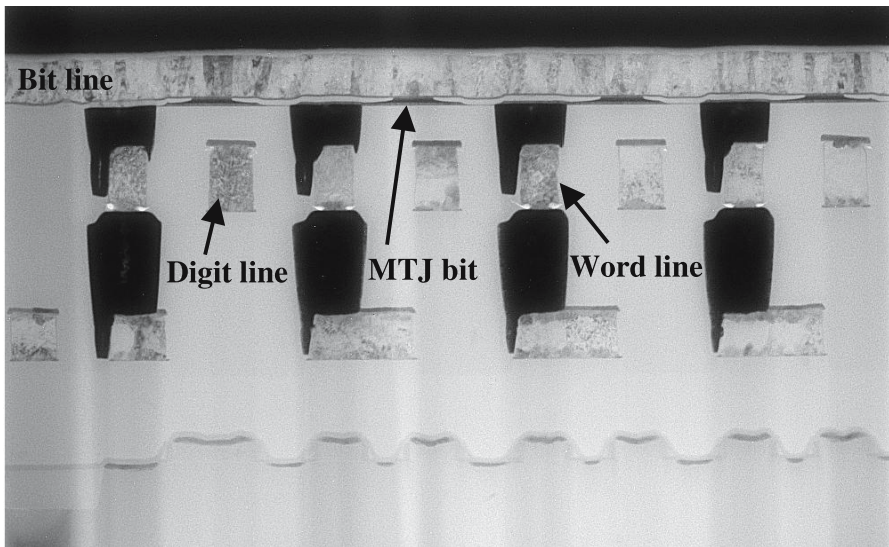
Fig. 7.8. Cross-section transmission electron micrograph of integrated MTJ MRAM (Courtesy of IBM Research)

read and write power consumption, due to the small aspect ratio cells and low sense current.

Although the large resistance and magnetoresistance are responsible for the above advantages over other MRAMs, if the cell resistance is too high, it will have an adverse effect on the read access speed. First, a high cell resistance requires a small current, as the maximum voltage drop across the cell must be less than the voltage supplied by the batteries. Hence, it requires a very quiet current source or a long average time for reading. Second, since the MTJ cell has capacitance, a high cell resistance means a long RC time constant. Obviously the cell resistance has to be optimized in actual design. In general, low RA product materials are needed for high-density MTJ MRAM.

Reading and writing: The reading and writing operations in 1MTJ/1T architecture are very similar to those in SV MRAM. As shown in Fig. 7.8, the word line connects the transistor in the cell to the MTJ element. Therefore, when a transistor is turned on, a sense current will flow from the bit line to the word line through the MTJ. Thus the resistance of the selected cell is sensed to read the memory state. Reading operation consumes only a small amount of power. For writing, the select transistor is not used. Currents flowing in the digit and bit lines generate a magnetic field required to switch the selected bit at the crossing of the lines. Since the MTJ cells do not need a large length-to-width aspect ratio for high signal, the required switching field is lower than in that SV or PSV MRAMs, which leads to relatively low power consumption in writing as well.

Challenges: No doubt MTJ MRAM offers attractive advantages over other MRAMs as just discussed; however, there are also unique challenges to overcome.

First of all, the tunnel resistance is very sensitive to both the insulating layer thickness and tunnel barrier height. Controlling the resistance uniformity over the whole wafer (which can be as large as 6 or 8 inches) is obviously a daunting task. The memory state of a cell is distinguished by the resistance level of the cell. Hence, to determine the memory state correctly, the cell resistance variation has to be much smaller than the difference in the resistance between the two memory states; i.e. the percentage variation of the resistance must be much smaller than the TMR of the MTJ material. Either the oxide barrier thickness or the barrier height can vary to cause a huge resistance variation; therefore, the Al-layer deposition and oxidation must be controlled extremely well. To achieve the high degree of the resistance uniformity, it first requires a very smooth substrate that the MTJ film is deposited on. Actual MRAM cells are built on wafers containing required CMOS circuitry; therefore the MRAM back end process must start with careful planarization to produce smooth surface. In addition, a reference cell has to be built next to the MTJ cell. When the active cell resistance is read out, it will be compared with the resistance of the reference cell, and then its memory state can be unambiguously determined. Very tight local resistance variation can be achieved [7.7] so that a meaningful comparison between the active and reference cells can be made. Another practical challenge unique to MTJ materials is the device yield. Electrical shorts across the very thin insulating layer can easily develop along the peripheral of a patterned MTJ element. This requires a very careful etching process in the patterning.

7.2.5 Other MRAM Concepts

Another type of MRAM that utilizes GMR materials in current-perpendicular-to-plane (CPP) geometry was proposed [7.29]. The memory cell of this vertical MRAM or VMRAM is a multilayered "doughnut-shaped" ring. The memory states are the clockwise and counterclockwise magnetization states. A dynamic read-out scheme similar to that used in PSV MRAM was proposed for reading. The magnetic switching mechanism is considerably different from that in other MRAM cells. In order to read and write the VMRAM cells, a tangential field is required. A double word and digit line design was proposed for generating the tangential field. Due to the inherently low signal level in all-metal GMR materials, the read access speed of the VMRAM will suffer until a very small cell size is reached. Another drawback is that the magnetic element alone (not the entire cell) would occupy at least $9F^2$ (F: minimum dimension in lithography), compared with $\sim 2F^2$ for a rectangular element.

Another proposed non-volatile RAM utilizes a single magnetic layer for storage and the Hall effect for reading [7.30]. The stray field of a single magnetic layer element is sensed by the Hall voltage of a two-dimensional electron or hole gas sheet underneath. Although the reading scheme is drastically different from the MR reading, the writing operation is essentially the same as other types of MRAM.
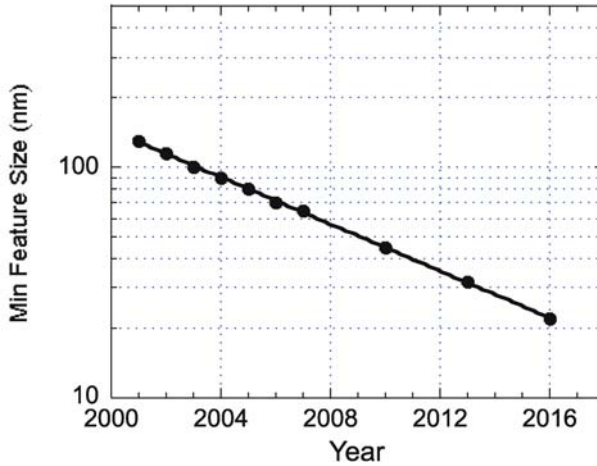
Fig. 7.9. Minimum feature size determined by semiconductor lithography vs. year for DRAM production (Data from ITRS 2001 report)

7.3 MRAM Cell Scaling

There are no adverse effects on the cell signal level as the MRAM cell size (not the length-to-width aspect-ratio) shrinks. However, the reduction in cell size drastically affects magnetic switching of the layer magnetization; therefore, it definitely affects the writing process. Although the reading operation does not involve any change to the magnetization state in the static read-out scheme, it does depend on magnetization rotation or switching in the dynamic read-out scheme. In addition, all the writing and reading operations using dynamic read-out rely on the half-select mechanism. It is very important to understand the magnetization reversal of the ever-shrinking MRAM elements under one or two orthogonal fields [7.31].

First of all, let us look at the general trend in DRAM cell scaling. If MRAM is to compete with DRAM, MRAM cell size has to be compared with the DRAM counterpart. Fig. 7.9 was plotted according to the latest data in the "The International Technology Roadmap for Semiconductors" or ITRS 2001 report for DRAM products [7.32]. The minimum feature size F refers to the "half-pitch" size in DRAM. This size is projected to pass the 100 nm mark in 2003 and continue to shrink steadily. The DRAM trend serves as a benchmark for future MRAM products, which means that the magnetic element has to shrink accordingly in future MRAM product generations.

In addition to the minimum feature size reduction that relies on the future advances in lithography technology, another quantity affecting the ultimate memory density is the "cell area factor". The absolute DRAM cell size ($C.S.$) is defined as $C.S. = a \cdot F^2$. The cell area factor, a, also decreases as F decreases according to the projected curve. This makes the packing density of the memory bits increase even more rapidly. For example, the area factor is eight in current product generation, but it will decrease to four when F reaches 32 nm. If MRAM is to follow the same trend, MRAM elements have to be packed more closely.

Let us not be concerned about technological challenges in making sub-100 nm magnetic elements in the next several product generations, but rather about possible fundamental limitations to MRAM scaling. In the 1970's and early 1980's, magnetic bubble memory, a type of non-volatile storage device, exceeded 1 Mb storage capacity, but it failed to compete with solid state memory devices or hard disks. The operation of the bubble memory devices was based on the formation and transport of bubble domains [7.33] in soft magnetic films such as epitaxial garnet films. The smallest bubble diameter in these films is about 0.3 μm. Clearly, the ultimate density is limited by the bubble domain size. As will be discussed in the following sections, as the magnetic element shrinks in future generations, it approaches the ideal single-domain. Fundamentally speaking, the higher-density MRAM elements are expected to perform much better in terms of magnetic switching and bit selection. No doubt, there are still challenging issues associated with very small memory devices, one of which is the superparamagnetic limit. In the next section, we focus on the switching characteristics of ideal single domains before reviewing experimental results on small patterned structures.

7.4 Coherent Rotation of Single-Domain Elements

7.4.1 Single-domain Size and Exchange Lengths

Magnetic domains exist in both hard and soft magnetic materials due to the magnetostatic (dipolar) interaction [7.34, 35]. In patterned magnetic elements, domain formation becomes less energetically favorable as the element size decreases because of the increasing cost in exchange energy. Eventually, below a certain size, called the single-domain size l_{SD}, the magnetic structures prefer to be single-domains. In general, l_{SD} depends on the physical shape and material parameters such as the exchange stiffness constant A, the saturation magnetization M_{s}, and the anisotropy constant K. The single-domain size and detailed "phase diagrams" have been numerically calculated with a broad range of anisotropy and various shapes [7.35].

The occurrence of magnetic domains depends on the element size compared with two fundamental length scales, both called exchange lengths, $l = \sqrt{A/K}$ and $l_D = \sqrt{A/2\pi M_{\mathrm{s}}^2}$. The first exchange length represents typical domain-wall width in an unpatterned film; the second exchange length represents typical size of a magnetization vortex core. In polycrystalline soft magnetic materials such as NiFe or NiFeCo, which are often used in MRAM, the anisotropy K is the induced uniaxial anisotropy that is set by an aligning field during film deposition. According to experimental data, this uniaxial anisotropy constant is about 10^3 erg/cm^3, equivalent to an anisotropy field of a couple of Oersteds. The energy scale associated with the demagnetizing field, $2\pi M_{\mathrm{s}}^2$, is about $5 \cdot 10^6$ erg/cm^3 in NiFe. If we take A=$1 \cdot 10^{-6}$ erg/cm, then the first exchange length l is approximately 300 nm and the second exchange lengthl_D is only about 4 nm. In structures whose lateral dimensions are much greater than l, the domains can be treated as different areas within which magnetization is uniform but between which the magnetization forms thin and abrupt boundaries, similar to

the crystallographic picture of a polycrystalline solid. Clearly, the patterned elements of interest are smaller than this length scale. This means that the magnetization continuously varies in a submicron element, just as within classical domain walls. In patterned soft magnetic materials, a more important length scale that determines domain formation is the second exchange length l_D. If the size of a magnetic element is below l_D, it will be in the single-domain state. The actual boundary between the single – and multi-domain or single-domain and vortex state may be several times large than l_D. Quantitative phase diagrams for patterned thin-film structures require detailed micromagnetic calculations.

In MRAM devices of many generations to come, the lateral dimensions are still much greater than the exchange length l_D, although the film thickness is comparable with the l_D. Although submicron and sub-100 nm MRAM elements are not truly single domains, we expect smaller devices to behave more like single domains. Next, we will consider the switching behaviors of single-domain elements.

7.4.2 Coherent Rotation of Single-domains with Uniaxial Anisotropy

Let us assume the magnetization in a small magnetic element to be uniform. In general, an ellipsoidal shape is considered so that both the magnetization and the demagnetizing field inside the body are uniform. For a sufficiently small element, the actual shape of the element is not important. For simplicity, we assume that the energy density has a well-defined second-order uniaxial symmetry. The uniaxial anisotropy can be a crystalline field anisotropy, induced anisotropy, magnetostriction, shape anisotropy or a combination of two or more anisotropy contributions. For a planar single-domain element of interest, we only need one parameter to represent the magnetization. The model based on this coherent or uniform magnetization rotation is called the Stoner-Wohlfarth (SW) model [7.36]. The free energy density is simply a sum of the uniaxial anisotropy and the Zeeman energy density due to the external field,

$$F_T = K \sin^2 \alpha - HM \cos \phi \ .$$
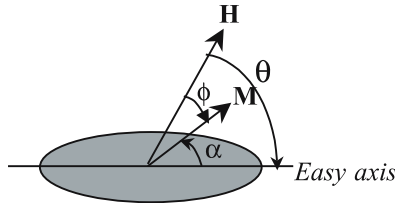
Easy-axis loop ($\theta = 0$, and $\phi = \alpha$). When the field is applied along the easy-axis direction, the total free energy density can be written as

$$F_T = K \sin^2 \phi - HM \cos \phi,$$

where the angles θ and ϕ are shown in the figure. For a given field H, a stable equilibrium direction of the magnetization can be found by minimizing F_T. First we have

$$\frac{dF_T}{d\phi} = 2K \sin \phi \cos \phi + HM \sin \phi = 0. \tag{7.1}$$

Denote $h \equiv \frac{H}{\left(\frac{2K}{M}\right)} = \frac{HM}{2K}$. Equation (7.1) has two solutions: $\sin \phi = 0$ and $\cos \phi = -h$. Then we can find which one is the stable solution, i.e. the minimum of the free energy density by examining the second order derivative,

$$\frac{d^2 F_T}{d\phi^2} = 2K \cos 2\phi + HM \cos \phi. \tag{7.2}$$

For the first solution $\sin \phi = 0$, $d^2 F_T/d\phi^2 = 2K(1 \pm h)$; the positive and negative signs correspond to $\phi = 0$ and $\phi = \pi$, respectively. $\phi = 0$ is metastable (i.e. $d^2 F_T/d\phi^2 > 0$) until h approaches -1 from the positive side. Likewise, $\phi = \pi$ is metastable until h approaches $+1$ from the negative side. When one angle becomes unstable, it jumps to the other. This jumping represents a magnetic switching event, and the corresponding reduced magnetic field is called switching field or critical field, h_c. Here we have, $h_c = \pm 1$.

For the second solution $\cos \phi = -h$, we have $d^2 F_T/d\phi^2 = 2K(h^2 - 1) \leq 0$. It represents an energy maximum, or an energy barrier separating the two minima. The energy barrier height is the difference between the maximum energy and the energy at the metastable state, and can be expressed by $\Delta = K(1 - |h|)^2$. Note that the energy barrier height is K in the absence of any easy-axis field, and it decreases quadratically as an easy-axis field is applied.

Now we can construct the easy-axis hysteresis loop. Fig. 7.10 shows the easy-axis normalized magnetization $\cos \phi$ vs. the reduced field h.

Hard-axis loop ($\theta = \pi/2$, $\alpha = \phi - \pi/2$). When an external field is applied perpendicular to the easy-axis, the total free energy density is, $F_T = K \cos^2 \phi - HM \cos \phi$. Let the first-order derivative be zero to determine the equilibrium angle,

$$\frac{dF_T}{d\phi} = -2K \sin \phi \cos \phi + HM \sin \phi = 0, \tag{7.3}$$

There are again two solutions: $\sin \phi = 0$ and $\cos \phi = h$. Then we examine the second-order derivative. For the first solution $\sin \phi = 0$, $d^2 F_T/d\phi^2 = -2K \cos 2\phi + HM \cos \phi$ is $2K(h - 1)$ when $\phi = 0$, and $-2K(h + 1)$ when $\phi = \pi$. It means that $\phi = 0$ is not stable until $h > 1$ and $\phi = \pi$ is not stable until $h < -1$. Both cases state one fact: the magnetization will be aligned along the field direction when the reduced field strength is greater than one.
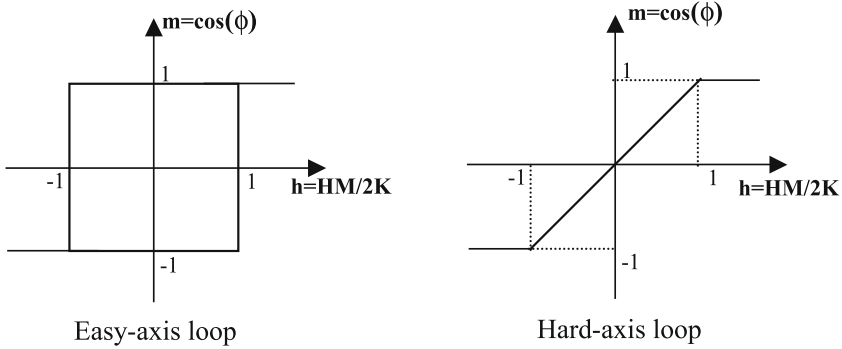
Easy-axis loop   Hard-axis loop

Fig. 7.10. Easy- and hard-axis hysteresis loop for planar single-domain elements with a unaxial anisotropy

For the second solution $\cos \phi = h$, we have $d^2 F_T / d\phi^2 = -2K \cos 2\phi + HM \cos \phi = 2K(1 + h^2) > 0$. Note that $|h| = |\cos \phi| \le 1$; therefore, this solution is always stable when $|h| \le 1$.

When a hard-axis field is applied, the hard-axis magnetization component increases linearly with the field strength until it saturates at $h_c = 1$, which is equal to the easy-axis critical field. A hard-axis hysteresis loop is also shown in Fig. 7.10.

Single-domain switching field with an arbitrary field angle. Above are two special cases when an external field is applied along the easy- or hard-axis. For an arbitary field direction, a numerical calculation is needed to construct the hysteresis loop. The critical field or switching field h_c can be solved by finding the instability point [7.36], i.e. by letting both first- and second-order energy derivatives vanish. The reduced switching field is expressed by,

$$h_c = \left(1 - w^2 + w^4\right)^{1/2} / \left(1 + w^2\right), \quad \text{with} \quad w = \tan^{1/3} \theta . \tag{7.4}$$

The switching field has a four-fold symmetry when the applied field direction is varied with respect to the anisotropy axis (Fig. 7.11). When $\theta = \pi/4$, it reaches the minimum at $h_c = 1/2$. In small magnetic elements, this perfect four-fold symmetry is rarely observed due to various reasons [7.37, 38].

In the SW model, switching of magnetization occurs at $h_c = 1$, or $H_c = 2K/M$. The absolute easy-axis switching field H_c is uniquely determined by the uniaxial anisotropy constant and the saturation magnetization. In small patterned magnetic elements, the predominant anisotropy is the shape anisotropy due to the strong demagnetizing effect. When the aspect-ratio is greater than one, the shape anisotropy can often be approximated by uniaxial anisotropy. Note that this approximation only applies to small elements in which nearly uniform magnetization prevails. Otherwise, the non-uniform magnetization tends to reduce the magnetostatic energy; therefore, the shape anisotropy is not a meaningful quantity. Let us consider a thin-film element with principal axes along x, y and z directions, the shape anisotropy energy density
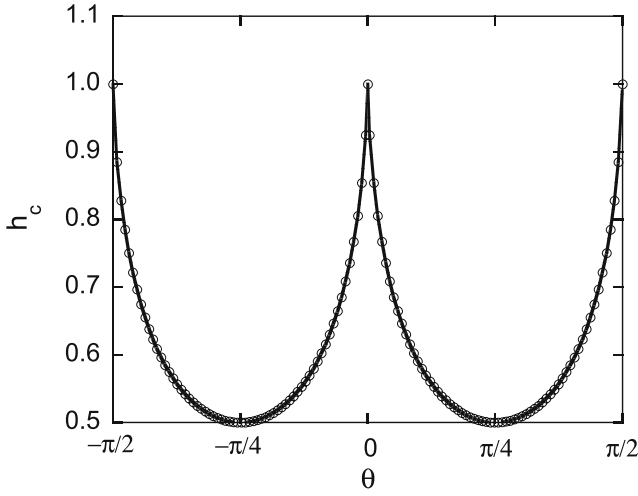
Fig. 7.11. Critical field as a function of the field angle for uniaxial planar single-domain elements

can be written [7.39],

$$F_D = \frac{1}{2} N_x M_x^2 + \frac{1}{2} N_y M_y^2 + \frac{1}{2} N_z M_z^2 \ , \tag{7.5}$$

where N_x, N_y, and N_z are three demagnetizing factors, and in CGS, $N_x + N_y + N_z = 4\pi$. If the long axis is along x-axis, and the film thickness is along z-axis, then we have $N_x < N_y < N_z$. If the field is in the x-y plane, the magnetization rotates in the x-y plane. Then we have,

$$F_D = \frac{1}{2} N_x M^2 + \frac{1}{2} (N_y - N_x) M_y^2 = \text{const} + \frac{1}{2} (N_y - N_x) M^2 \sin^2 \alpha \ . \tag{7.6}$$

If we ignore the unimportant constant term in the demagnetizing energy density, we can identify the uniaxial anisotropy constant, $K = \frac{1}{2}(N_y - N_x) M^2$. For an ellipsoid with semi-axes a, b, and c along x, y and z directions respectively, the demagnetizing factors can be found for various cases. For $a \geq b \gg c$, i.e. a very flat ellipsoid [7.40], the demagnetizing factors contain elliptic integrals, but N_x and N_y depend on the ratio c/a, and parameter $e = (1 - b^2/a^2)^{1/2}$. For a small patterned thin film element with length L, width W, and film thickness t, the switching field H_c can be approximately written as,

$$H_c = \frac{t}{W} f \left(\frac{L}{W} \right) \ . \tag{7.7}$$

7.4.3 Switching Astroid

In a 2D array of MRAM cells, switching of a selected cell is always done by two fields. Let us first understand how single domains switch under a pair of orthogonal fields.

We choose the easy- and hard-axes of a uniaxial planar single-domain element as the x- and y-axes. If two independent fields, H_x and H_y, are simultaneously applied, the total free energy density is,

$$F_T = K \sin^2 \alpha - H_x M \cos \alpha - H_y M \sin \alpha . \tag{7.8}$$

Again we will determine the switching field by setting both the first- and second-order derivatives to zero,

$$\frac{\mathrm{d}F_T}{\mathrm{d}\alpha} = 2K \sin \alpha \cos \alpha + H_x M \sin \alpha - H_y M \cos \alpha = 0 , \tag{7.9}$$

$$\frac{\mathrm{d}^2 F_T}{\mathrm{d}\alpha^2} = 2K \cos 2\alpha + H_x M \cos \alpha + H_y M \sin \alpha = 0 . \tag{7.10}$$

We again define the reduced fields, $h_x = H_x M/2K$ and $h_y = H_y M/2K$. From the above two equations, we obtain the following reduced switching fields:

$$h_{xc} = -\cos^3 \alpha, \quad h_{yc} = \sin^3 \alpha, \quad \text{or} \quad h_{xc}^{2/3} + h_{yc}^{2/3} = 1 . \tag{7.11}$$

Equation (7.11) represents the well-known Stoner-Wohlfarth switching astroid (SW astroid) [7.36]. If there is only an easy-axis field, the critical field is one. The easy-axis switching field decreases from one, as an orthogonal field component is present. The same message is contained in the previous h_c vs. θ curve. The SW astroid not only determines whether switching occurs in the presence of a pair of orthogonal fields, but also graphically shows the metastable magnetization directions [7.41] (Fig. 7.12). If you draw a tangent to the astroid from a tangential point to the endpoint of the field vector $\boldsymbol{h} = (h_x, h_y)$ for any given point inside the astroid (i.e. below the switching threshold), then the direction of the vector is the equilibrium magnetization direction, represented by angle the α. The hysteresis loops can be constructed by finding the α value graphically, or by solving (7.9) numerically. A series of hysteresis loops is shown in Fig. 7.13.

The switching astroid is a wonderful benefit for selectivity. If the switching threshold did not depend on the applied field direction, the half-select scheme would still work. Each line would then need to supply 71% (or $1/\sqrt{2}$) of the required switching field to switch the selected cell and a single line would not affect the half-selected cells. Since the switching threshold varies with the field orientation according to the SW astroid, the minimum field strength needed is $h_c = \sqrt{h_{xc}^2 + h_{yc}^2} = 1/2$ instead of one, and we have $h_{xc} = h_{yc} = 2^{-3/2} = 0.35$. In other words, each line needs only 35% (or $(1/\sqrt{2})^3$) of the full switching field to switch the selected cell! Therefore, the half-selected cells have a much smaller probability to be switched since they only see 35% of the required full switching field. If there is additional anisotropy present, then the switching astriod can be more complex. In general patterned MRAM elements do not follow the SW astroid.
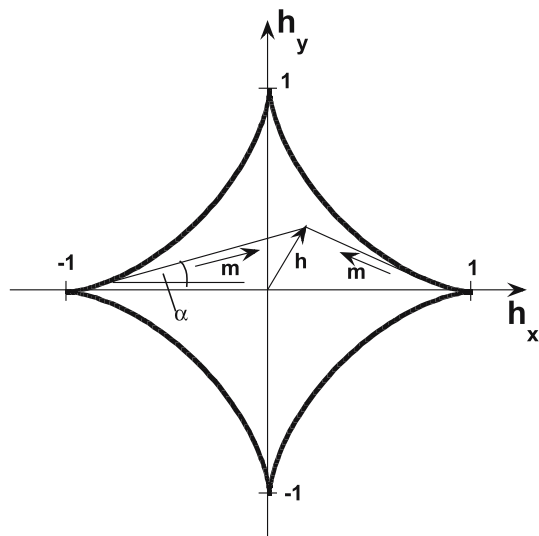
Fig. 7.12. SW switching astroid for single-domain elements. For any field h, the vector linking the tangential point on the SW curve to the endpoint of h vector represents the metastable magnetization direction. There are two metastable magnetization directions, but the actual magnetization direction depends on the initial magnetization state
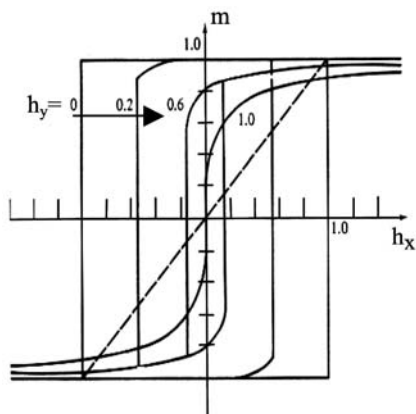

Fig. 7.13. Easy axis hysteresis loops with various hard-axis field values for unaxial single-domain elements

7.5 Switching of Submicron MRAM Devices

7.5.1 Single-domain-like Switching Characteristics

Submicron and sub-100 nm MRAM devices are still greater than the single-domain size; therefore, in many product generations to come, we do not expect the coherent switching to occur as described by the SW model. On the other hand, we also know that
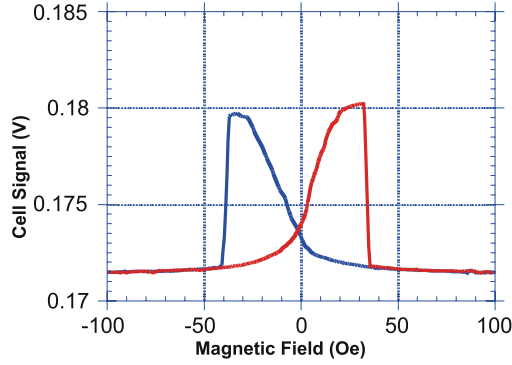
Fig. 7.14a. Magnetoresistance of a 1 µm×10 µm PSV MRAM device. At high field strength, magnetzation of both layers are aligned by the external field. Because of the differential coercive fields (for 4 and 6 nm thick NiFeCo respectively), as the field reverses the direction, the thin layer magnetization, creating an anti-parallel configuration. In this device, the anti-parallel state is not fully reached
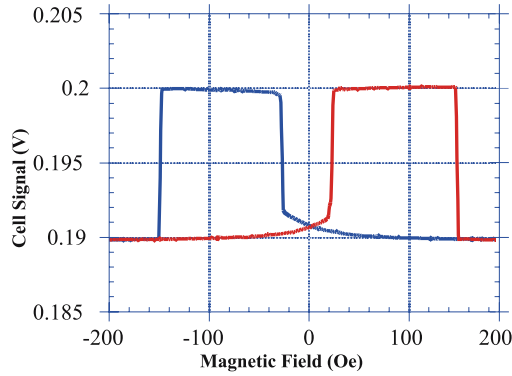
Fig. 7.14b. Magnetoresistance of a 0.25 µm×2.5 µm PSV MRAM device patterned from the same PSV film as used in Fig. 7.14aa. Complete parallel and anti-parallel alignments are realized as indicated b the resistance plateaus

the device lateral dimensions are comparable with or smaller than the first exchange length, i.e. the length scale characterizing the width of a domain-wall in unpatterned soft magnetic films. In general, the switching characteristics of submicron devices are expected to be much simpler than those of the large structures whose switching is dictated by the motion of domain walls. This point is nicely illustrated by two PSV MRAM devices [7.20] (Fig. 7.14a). The two constituent magnetic layers of a PSV film differ only in the thickness. The coercive field of an unpatterned film is not sensitive to its thickness; consequently, the unpatterned PSV films do not show any GMR because no anti-parallel magnetization alignment can be realized by an applied field. When patterned to 1 µm × 10 µm stripes, the PSV layers start to show different coercive fields, with the thick film switching at a higher field. There are two peaks
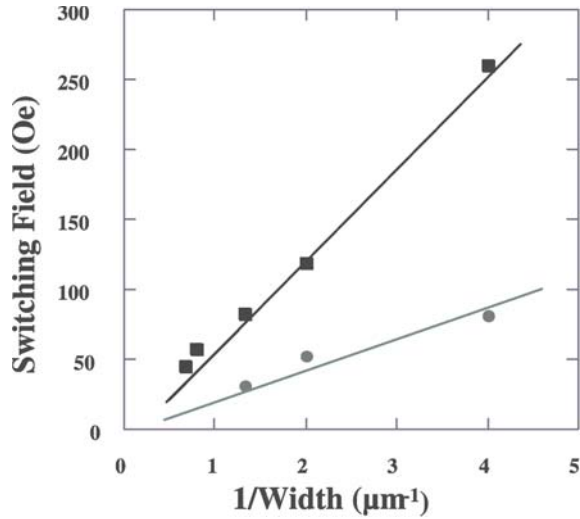
Fig. 7.15. Switching fields of two layers in PSV MRAM devices. Similar inverse relationships have been observed in submicron SV MRAM devices and single-layer elements
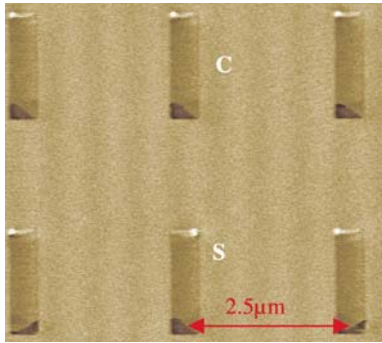

Fig. 7.16. Magnetic force microscopy (MFM) image of patterned submicron NiFe elements. The end-domain state can be either "C" or "S"

in MR traces, caused by some degree of anti-parallel alignment (Fig. 7.14a). When the device width reaches 0.7 μm or so, the switching characteristics are qualitatively different. The MR vs. field traces become very squared. In a 0.25 μm × 2.5 μm device (Fig. 7.14b), both the thick and thin layers switch abruptly, and moreover, they switch between two well-defined magnetization states as suggested by the plateaus. This is indicative of the easy-axis single-domain-like switching characteristics. In addition, the switching field of both films is found to be inversely proportional to the element width for a fixed length-to-width aspect-ratio (Fig. 7.15), which is consistent with the SW coherent switching model (7.7).

On a submicron scale, patterned MRAM devices clearly possess well-defined shape anisotropy and stable single-domain-like remanent states. Systematic stud-

ies have also shown that when the film thickness is small compared with l_D, the switching field of submicron single-layer elements follows the above inverse relationship well [7.42]. As the thickness increases, more deviation from the inverse relationship is developed. It is attributed to the increased magnetostatic energy in thick film elements, which is usually the driving force for domain formation. The remanent state of submicron elements, especially those with large aspect ratio, is generally characterized by uniform magnetization except at the element ends. These end domains (we reserve the terminology "edge domains" for domains in edge-pinned states) can have "S" and "C" configurations (Fig. 7.16), which refer to the parallel and anti-parallel transverse magnetization at two ends respectively. In long aspect-ratio elements, the partial flux-closure end domains do not affect the shape anisotropy as much as in small aspect-ratio elements for quite obvious reasons. In small aspect-ratio elements, the end domains cause the anisotropy to deviate from the uniaxial symmetry; consequently, they have greater impact on the magnetization-reversal [7.42].

7.5.2 Switching Irreproducibility

Submicron MRAM devices appear to work like single-domain objects. According to the SW model, the easy-axis switching field depends only on the device geometry and the magnetization. However, the switching field of submicron devices is not always reproducible and the irreproducibility is often found in thick PSV devices. In PSV films, the thin layer is typically 3–4 nm thick and the thick layer 6–9 nm thick. Even for identical field sweeps (field range, sweeping rate, etc.), the switching of the thick layer occurs unpredictably from sweep-to-sweep, but it often shows a discrete distribution (Fig. 7.17a). The distribution varies from device-to-device on the same wafer even though they are made identical. This kind of switching anomaly is inconsistent with the single-domain picture.

An interesting fact about this anomaly is that those seemingly "ill-behaved" devices work perfectly if the range of field sweeps is expanded (Fig. 7.17b). But when going back to the narrow range is restored, the same anomaly reappears. By "overdriving" the devices, good switching reproducibility can be readily achieved. It is worth noting that this approach would not work for MRAM devices, because the overdriving field would switch all half-selected devices so that the selectivity is completely lost.

This type of anomaly actually provides us some insights about the micromagnetic "defects" developed in those seemingly single-domain structures. First, the "defects" cause the switching to vary. Second, they appear in a rather unpredictable way. In addition, the remnants of the "defects" can be swept out by increasing the magnetic field strength. Similar anomalous behavior also exists in small aspect-ratio MTJ MRAM devices when the free layer is made of thick films (Fig. 7.18).
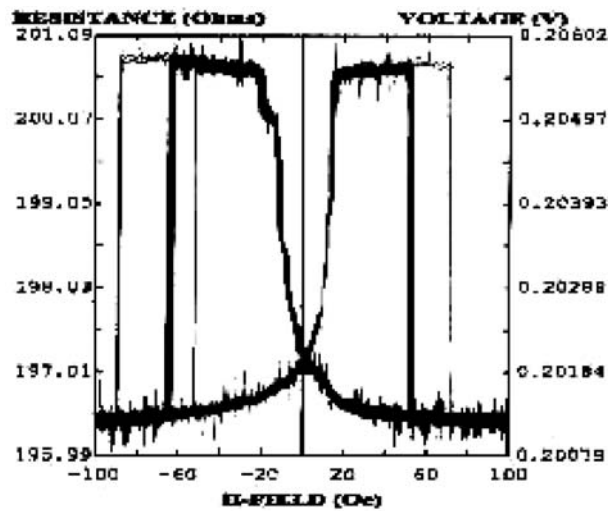
Fig. 7.17a. Magnetoresistance of a 0.5 μm×5 μm PSV MRAM device (overlay of 40 identical continuous field sweeps). The switching field of the thick layer can vary by a factor of two in many similar devices
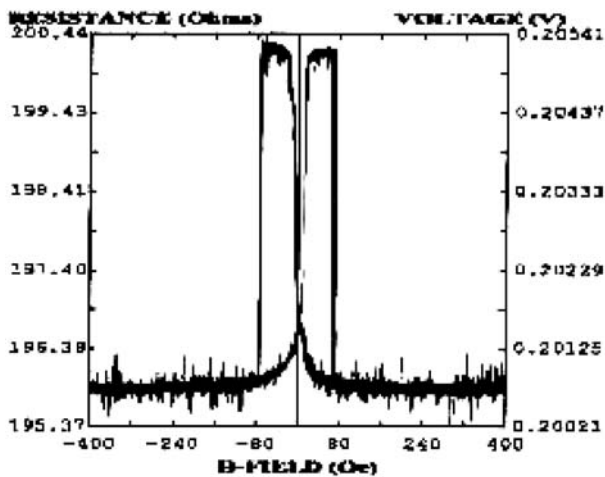

Fig. 7.17b. Magnetoresistance of the same device shown in Fig. 7.17a (also 40 sweeps). The range of the field sweeps is increased by a factor of four. The switching of the thick layer magnetization is perfectly reproducible
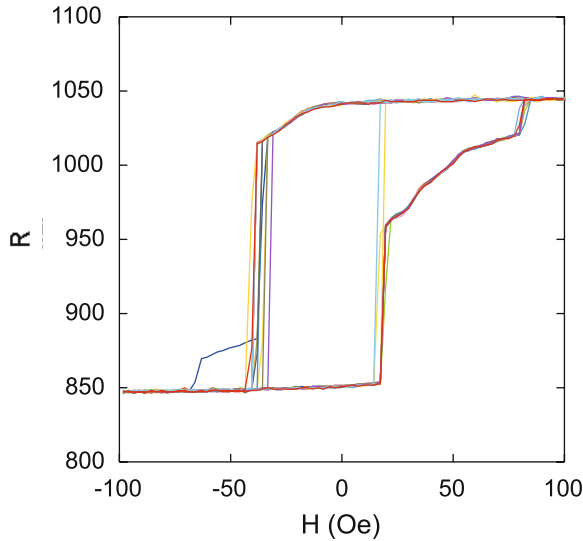
Fig. 7.18. TMR of a 0.9 µm×1.5 µm MTJ MRAM device (12 sweeps). The free layer is about 6 nm thick

7.5.3 Hard Axis-loops

The hard-axis loops of submicron elements appear somewhat like the SW model predictions, but differ in detail. First, if the hard-axis loop is compared with the easy-axis loop, the saturation field in the hard-axis direction is often greater or much greater than the easy-axis switching field. This is the case in a variety of submicron and deep submicron patterned elements [7.43] (e.g. in Fig. 7.19. According to the SW model, the critical field has a four-fold symmetry in the field angle; therefore, the easy- and hard-axis critical field should be equal for uniaxial single-domains. This discrepancy is often ascribed to the non-coherent mechanism in magnetization reversal. In the hard-axis direction, the saturation field is a measure of the anisotropy. When an easy-axis field is applied, local nucleation always takes place instead of coherent rotation so that the switching process does not have to go over the anisotropy barrier. This argument is essentially the same as the one used for the case of Brown's paradox [7.44, 45].

Second, there is always a small amount of hysteresis in the hard-axis loop. In short aspect-ratio elements, the hard-axis loop can be very significant. The finite hard-axis loop also contradicts the uniaxialsingle-domain model. In nearly single-domains, the hard-axis remanence is due to end-domains whose magnetization is transverse to the easy direction. At the end of each hard-axis field sweep, the end-domain magnetization is left in that field direction. From one end-domain state to the other equivalent state, there is a barrier to overcome, which consequently produces a hard-axis loop. Different end-domain states can result in different switching behaviors in easy-axis field sweeps. Hence, the hard-axis remanence is undesirable but unavoidable in submicron MRAM devices.
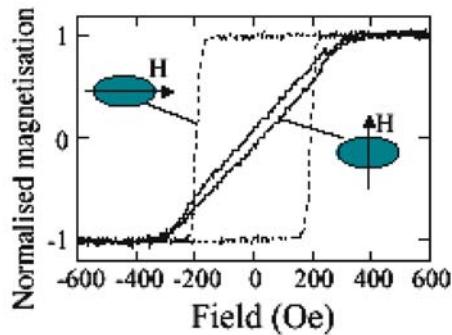
Fig. 7.19. Easy- and hard-axis hysteresis loops of an array of elliptical supermalloy elements. The major- and minor-axis lengths are 250 nm and 125 nm respectively, and the film thickness is 10 nm (Data from [7.43])

7.5.4 Deviation from the SW Astroid

The easy- and hard-axis behavior already implies that the submicron MRAM devices do not follow the ideal SW astroid. Along the hard-axis direction the observed astroid is usually elongated. The degree of this elongation is lessened in small elements. The experimental astroid of a PSV MRAM device shown below (Fig. 7.20a) displays a significant deviation from the standard SW astroid, which would result in an ineffi-cient bit selection. In devices that show anomalous switching as discussed previously, the astroid would have multiple branches along the easy-axis. However, the general trend is that the astroid curves approach the SW curves as the size of the element shrinks (Fig. 7.20b). This is good news in terms of switching selectivity. It should be pointed out that having nice and reproducible easy-axis switching characteristics is necessary but not sufficient for bit selection.

Hard-axis field sensitivity is generally poorer for small aspect-ratio rectangular elements [7.46]. An example is given for a single-layer NiFe rectangular element array (Fig. 7.21). The easy-axis switching field shifts only about 1 Oe for every 10 Oe hard-axis field increment. The square element case is a disastrous extreme. Because of the four-fold symmetry in square elements, the usual half-select scheme stops working even if they are perfect single-domains. In general, the h_y vs. h_x "astroid" is much more complex than the SW astroid if the anisotropy is not purely uniaxial.

7.6 Micromagnetic Properties of Submicron MRAM Devices

Switching anomalies discussed in the last section are clearly related to non-uniform magnetization in submicron elements. Non-uniform magnetization states are devel-oped because the magnetostatic energy is lower than that of the uniform state. If the magnetization varies locally, the magnetostatic energy does not depend solely on the shape of the elements, but on the actual configuration or spatial variation of the
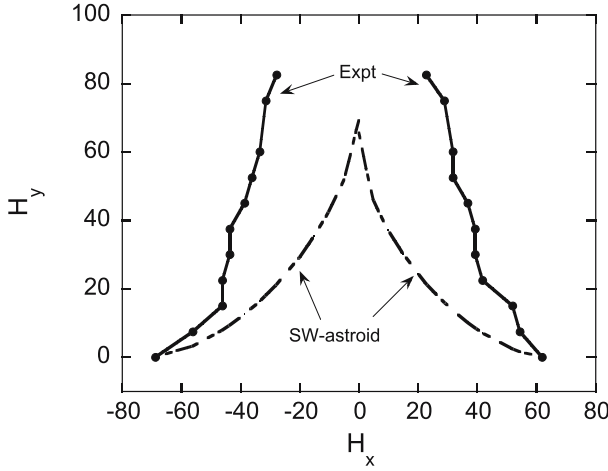
Fig. 7.20a. A half switching astroid for a 0.6 μm×6 μm PSV device. The experimental curves are severely stretched vertically. To reduce the switching field of the selected bits in an array, a very high hard-axis field is needed.
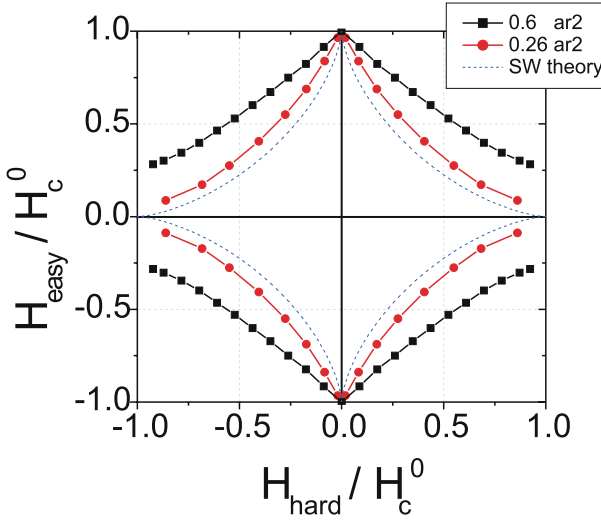

Fig. 7.20b. Simulated SW astroids for 0.6 μm and 0.26 g μm wide elements (aspect ratio = 2). The behavior of the 0.26 μm element is closer to the SW theory prediction. The simulation was done by solving Landau-Lifshitz-Gilbert equation. Note that the easy- and hard-axes are switched (Courtesy of Motorola Labs)

magnetization. The equilibrium magnetization configuration will be settled in a minimum energy state. Unlike single-domains, there can exist multiple minimum energy states. The final state depends on the actual path that the magnetization takes (related to field history) and the thermal fluctuations near the critical field. Computing static
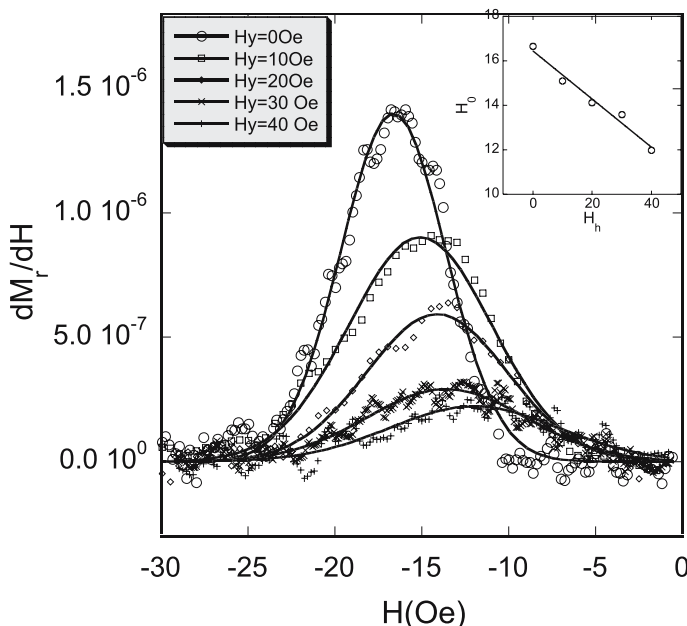
Fig. 7.21. $dM_r\,dH$ vs. H for an array of $0.9\,\mu m \times 1.2\,\mu m$ NiFe elements with different hard-axis fields. M_r is the magnetization remanence measured as a function of reversal field. The solid lines are Gaussian fits. The Gaussian center moves to lower fields as the hard-axis field increases, while the standard deviation of the Gaussian distribution increases slightly. The inset shows the Gaussian center as a function of the hard-axis field

and dynamic magnetization configurations as well as magnetic hysteresis loops is an objective of "micromagnetics", which is reviewed by Arrott in a separate chapter. The subject of micromagnetics has been a rapidly developing field in the past several years due to the growing interest in MRAM. In this section, we will discuss the micromagnetic properties of patterned elements related to the switching anomalies described earlier.

7.6.1 Trapped Magnetization Vortices

A common form of micromagnetic "defects" in nearly single-domain structures is magnetization vortices. Since all three dimensions of a submicron MRAM element are greater than or comparable with the exchange length l_D, i.e. the vortex core size, the vortex plays an important role [7.47] in submicron and sub-100 nm MRAM devices. Magnetization vortices can be locally trapped in an element at remant states. In large aspect-ratio elements where the uniaxial anisotropy dominates, the remanent state even with trapped vortices still has well-defined overall magnetization. Since a trapped vortex causes only a local disturbance to the nearly uniform magnetization, the deviation from the full saturation magnetization is often hidden in the tail of the hysteresis loop. Magnetization remanence measurements can reveal the trapped
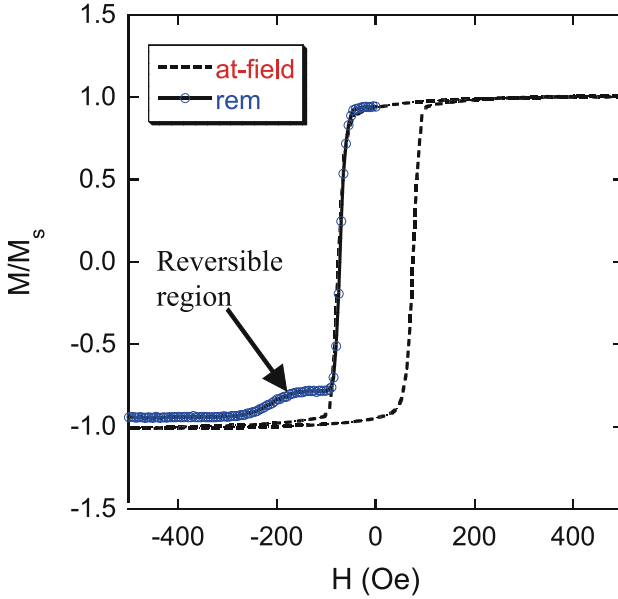
Fig. 7.22. Normal hysteresis loop vs. magnetization remanence curve of 30 nm thick 0.9 μm×4.5 μm NiFe patterned array. In the plateau region, the magnetization is reversible. "At-field" curve is the regular hysteresis loop, and "rem" is the remanence curve

vortices, for there is always a reversible component in the magnetization when a vortex is pushed away from the equilibrium position (Fig. 7.22). On the remanence curve, the magnetization has a plateau before the vortices are driven out of the elements [7.48].

Although the remanent states with trapped vortices in large aspect-ratio elements can still serve as memory states, the trapped vortices greatly affect the magnetization reversal [7.49, 50]. Two strikingly different hysteresis loops from the same array of patterned elements are shown in Fig. 7.23. One loop is taken between two end fields where magnetization is fully saturated; the other is between two end fields that would correspond to the plateau region on the remanence curve, i.e. trapped vortex region. When a hysteresis loop starts from the plateau region, it exhibits two-step switching, denoted by the respective fields, H_{c1} and H_{c2}. In fact, H_{c2} is the same as the switching field of the major loop, but H_{c1} is much smaller. Since this is a measurement over a collection of nominally identical patterned elements, the two-step switching points to two possibilities: either each element switches in two steps, or the element array divides into two separate groups having different switching fields.

Magnetic force microscopy (MFM) imaging clearly supports the latter case (Fig. 7.24). Zero-field MFM reveals two types of magnetization configurations: with and without trapped vortices. The relative ratio between the two types varies with the initial condition or the field that prepares the initial state. MFM tracking of a same group of elements under a varying field has confirmed that the elements with trapped vortices switch at a lower field [7.50]. We also found after each sweep that the
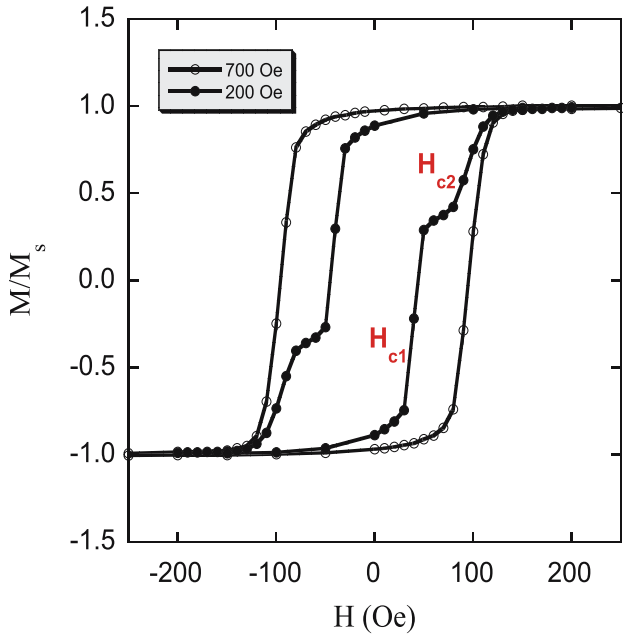
Fig. 7.23. Two representative hysteresis loops of 20 nm-thick 1 μm×5 μm NiFeCo patterned array. When the two end-fields are below 300 Oe, the hysteresis loops has two steps. This is true for element widths down to 0.2 μm

presence of the trapped vortices in the same element group is probabilistic, but the percentage of elements with trapped vortices varies with the end-field of the previous field sweep. As the end-field increases, the vortex population decreases progressively until all elements are free of trapped vortices (Fig. 7.25). To eliminate the "nuclei" of reversal domains, a high field is required to ensure reproducible switching. This is reminiscent of the switching anomaly in single PSV devices.

The microscopic process associated with the anomalous switching is further corroborated by Landau-Lifshitz-Gilbert (LLG) micromagnetic simulation [7.50]. In Fig. 7.26, the simulation was carried out for an element with the same geometry as that in Fig. 7.24. State "a" is the remanent state from a high field; state "b" is the remanent state from an intermediate field where the full saturation has not been reached. State "b" corresponds to the tail region on the remanence curve. Although the remanent state still retains almost full magnetization, it contains two trapped vortices. Starting from these two states, the subsequent switching takes place at two different fields (Fig. 7.27).

The anomalous switching in PSV MRAM devices has also been simulated using LLG micromagnetics. Trapped magnetization vortices in the thick layer can indeed cause switching field to vary from sweep-to-sweep (Fig. 7.28). The micromagnetic simulation results qualitatively agree with the experimental data in PSV devices.
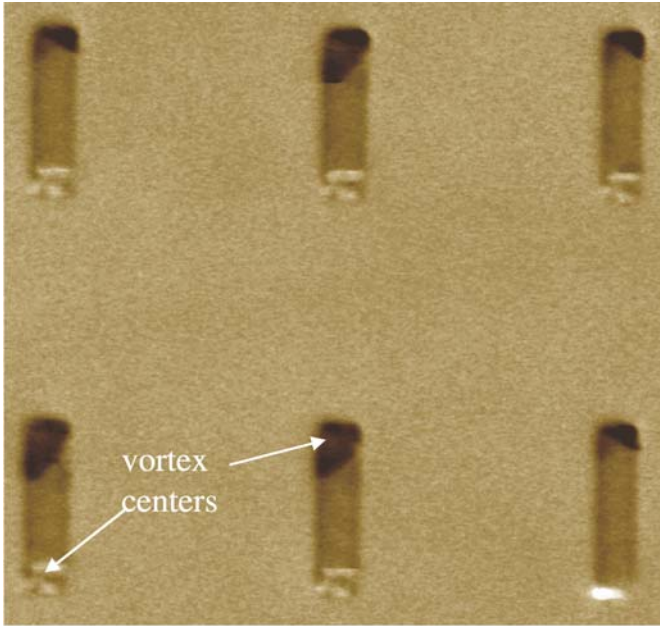
Fig. 7.24. MFM image of the patterned elements used for Fig. 7.23. It is an image of a remanent state from an intermediate field (about 150 Oe). Although the magnetization of all elements has reversed from their initial direction, most elements have one or two trapped vortices

Vortices in small aspect-ratio MRAM devices can not only cause switching field variation as shown in Fig. 7.18, but also a complete loss of memory states if the vortices are trapped. For MRAM devices, magnetization vortices seem to always adversely affect magnetization switching and should be avoided at all cost. Recently, "doughnut" or ring geometry, similar to the ferrite-core, has been proposed to utilize the two senses of a magnetization vortex as two memory states in VMRAM. Then, the goal in VMRAM is just the opposite: a stable vortex state must always be maintained.

Magnetization vortices in both large and small aspect-ratio patterned elements have recently been studied by many researchers [7.47, 51–55] (e.g. Fig. 7.29). In general, the thicker the film (compared with l_D) is, and the smaller aspect-ratio the patterned device has, the more energetically favorable trapped vortices become. A magnetization vortex "phase diagram" [7.52] such as Fig. 7.30 can be used as a guide to prevent trapped vortices in various structures.

7.6.2 Edge-Pinning

The edge-pinned state is another non-uniform magnetization configuration often found in submicron devices. In particular, when a hard-axis field promotes the center of the element to rotate first, the long edges resist rotating in unison with the center to avoid high "pole" density. As a consequence, the edge-pinned state or edge-domain
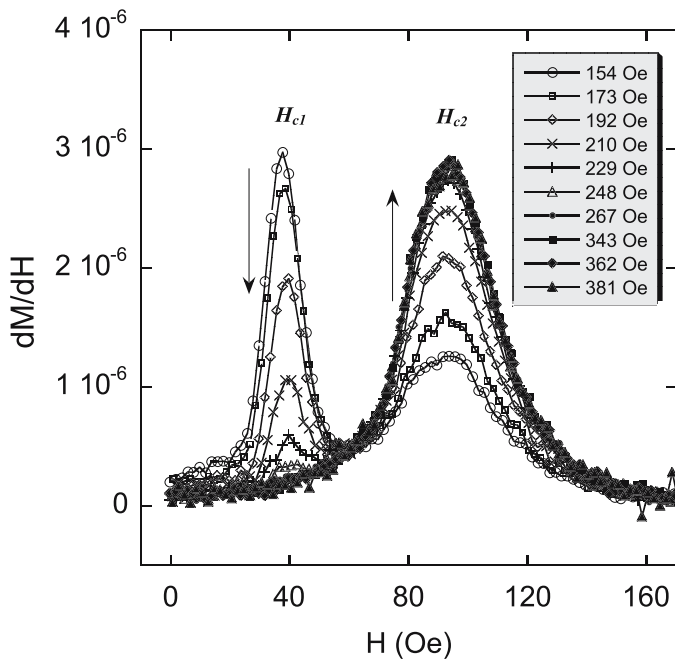
Fig. 7.25. dM/dH data from a series of hysteresis loops for NiFe elements used in Figs. 7.23 and 7.24. The initial state was a demagnetized state. Then regular hysteresis loops are taken with an increasing range of field sweep (shown in legend). As the field range expands, the low-field portion progressively decreases until all elements switch at H_{c2} as the field reaches about 300 Oe.

state is preferred (Fig. 7.31, simulated using LLG Micromagnetics Simulator [7.56]). Although the center magnetization is reversed, the edge-pinned state may not be a fully reversed state [7.46, 57]. Full switching of the memory state depends on the switching of the pinned edges, which starts at corner spins. Once the corner spins are depinned, it triggers an avalanche of the edge spin reversal. This edge wall propagation, similar to the motion of a soliton, takes place rather effortlessly shown by micromagnetic simulations.

7.6.3 360 °C Domain Wall

For long-aspect ratio elements relevant to PSV MRAM devices, the "C" state reversal can result in trapped 360 °C domain walls [7.58], according to micromagnetic simulations. This metastable state also causes the switching field to vary. Since the 360 °C wall formation is caused by "C" end domain initial state, it can in principle be eliminated by a hard-axis field which always forces the end domains to be biased toward an "S" state. In small aspect-ratio elements relevant to MTJ MRAM, the 360 °C domain wall is less likely.
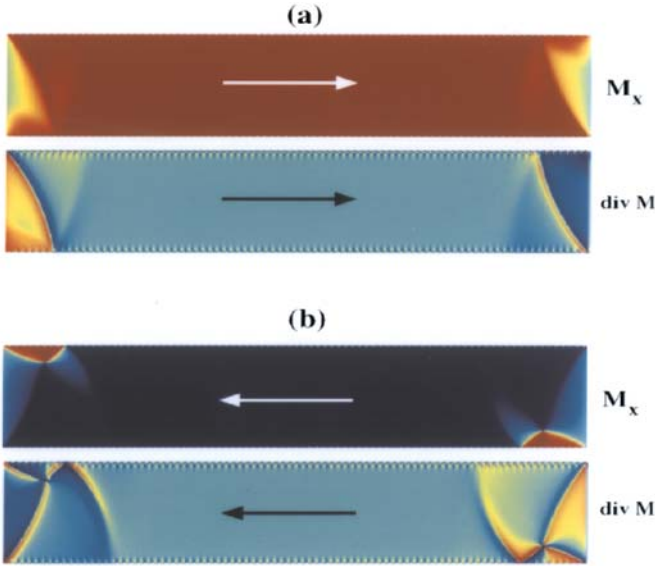
Fig. 7.26. Easy-axis magnetization component (M_x) and magnetization (div**M**) divergence from micromagnetic simulation. The div**M** patterns can be directly compared with the MFM images. The element is 20 nm thick 1 μm×5 μm NiFeCo. States "a" and "b" are two remanent states in the hysteresis loop shown in Fig. 7.27

7.6.4 Effect of Element Shape

In small devices, the local charge density $\sigma = M \cdot \widehat{n}$; therefore, the magnetostatic energy becomes increasingly dependent upon the element shape. This shape sensitivity actually offers some degree of flexibility to tailor desired magnetization configuration and switching characteristics. This "shape engineering" or "micromagnetic engineering" has been investigated by many researchers [7.43, 51, 58, 59]. One direct consequence of shape variation is the effect on the demagnetizing field, and therefore on the switching field (Fig. 7.32). The switching field can be drastically increased if a sharp end is introduced. Another consequence is the influence on the switching modes of the elements. For example, an asymmetric shape can be used to bias the magnetization toward the "C" state; therefore, the element will not switch unless a hard-axis field is simultaneously present. In other words, a steep switching astroid can be engineered to achieve perfect selectivity [7.60]. However, the second aspect of shape control will become less effective when the dimensions of the element approach single-domain size.
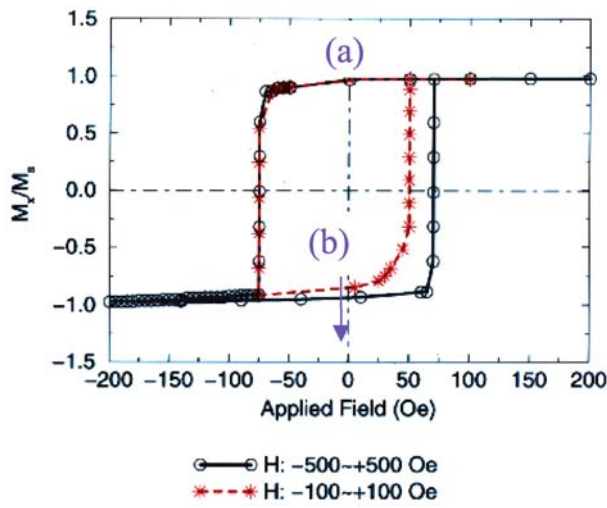
Fig. 7.27. Simulated hysteresis loops with different field sweep ranges. One loop (open circles) starts from 500 Oe, to −500 Oe, and then returns to 500 Oe. After the first sweep ends at 500 Oe, the field is set to 100 Oe. The second loop (crosses) starts from 100 Oe, to −100 and then returns to 100 Oe. The magnetization configurations at states (**a**) and (**b**) are shown in Fig. 7.26
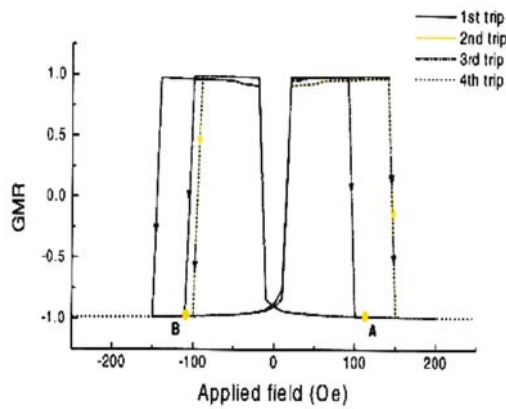

Fig. 7.28. Micromagnetic simulation for a PSV MRAM device. Trapped vortices can produce switching field variations (Courtesy of J.-G. Zhu).

7.7 Issues Related to Magnetic Switching in Future High-Density MRAM

7.7.1 Interlayer Magnetostatic Coupling Due to End Charges

To achieve high density, the cell aspect ratio needs to be small. Unlike PSV materials, MTJ materials do not need large aspect-ratio to boost signal level. Hence, the aspect-ratio requirement has no fundamental effect on reading. However, a small aspect-ratio
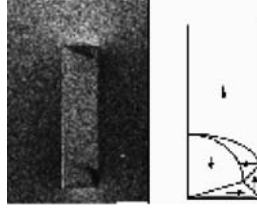
Fig. 7.29. Lorentz microscopy image of a patterned NiFe element. A trapped vortex is present at one end of the submicron element (Data from [7.51])
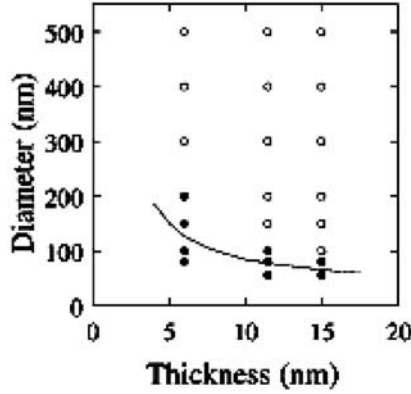

Fig. 7.30. Vortex phase diagram for patterned Supermalloy disks. Solid dots represent the vortex-free state and open circles the vortex state (Data from [7.52])
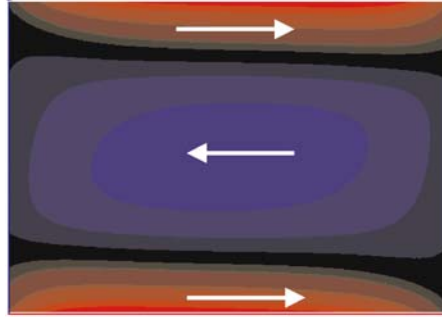

Fig. 7.31. Simulated edge-pinned state in a 5 nm thick $0.9\,\mu\text{m} \times 1.2\,\mu\text{m}$ NiFe element.

element produces a stronger longitudinal demagnetizing field, H_d. By definition, this demagnetizing field is anti-parallel to the magnetization inside the element. Immediately above and below the element, the tangential component of the field must be continuous; therefore, it is also anti-parallel to the layer magnetization and its strength increases in small aspect-ratio elements. In a sandwich structure used in MRAM, this demagnetizing field acting on the other layer can be so strong
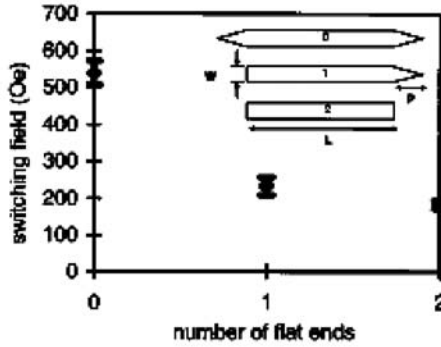
Fig. 7.32. Effect of sharp features on switching field. The width of all elements is 200 nm (Data from [7.51]).

that it always keeps the magnetization of the other layer anti-parallel to its own magnetization. Likewise, the other layer's demagnetizing field also reinforces this anti-parallel coupling. Hence the stable remanent configuration of small aspect-ratio elements tends to be the anti-parallel state (Figs. 7.33 and 7.34) [7.61]. This puts a shift in the free-layer hysteresis loop. If the demagnetizing field is larger than the coercive field of the thin layer, the free-layer loop is completely off center, causing a loss of the other memory state. In PSV devices where both magnetic layers are required to switch, the magnetostatic coupling further increases the switching field of the thick layer. This demagnetizing field varies approximately with $1/(\text{length})^2$ for a fixed element width [7.61]. To minimize this magnetostatic bias on the free layer, a pair of antiferromagnetically coupled layers such as Co/Ru/Co can be used. In the Co/Ru/Co sandwich, flux is almost closed between the two Co-layers; therefore, the bias on the free layer can be effectively reduced.

7.7.2 Interlayer Néel Coupling Due to Interfacial Charges

In increasingly small MTJ MRAM devices, a thinner oxide layer has to be used to reduce the tunneling resistance (for small RC constant). Due to the unavoidable interfacial roughness, the Néel coupling or orange-peel coupling between the two magnetic layers increases drastically. This coupling favors a parallel alignment between the two layers as schematically shown below. In a simple analysis [7.62], the coupling strength, H_{cpl}, is related to the amplitude and wavelength of the interfacial roughness (7.1). This analysis can be extended to a more complex situation involving many layers in MTJ stacks [7.63]. For a thin free-layer with a thin oxide layer, this coupling can also put the hysteresis loop completely off center.

$$H_{\text{cpl}} = \left(\frac{\pi^2 h^2 M_P}{\sqrt{2}\lambda \cdot t_F} \right) \cdot \exp\left(-2\pi\sqrt{2} \cdot t_s/\lambda \right) \tag{7.12}$$
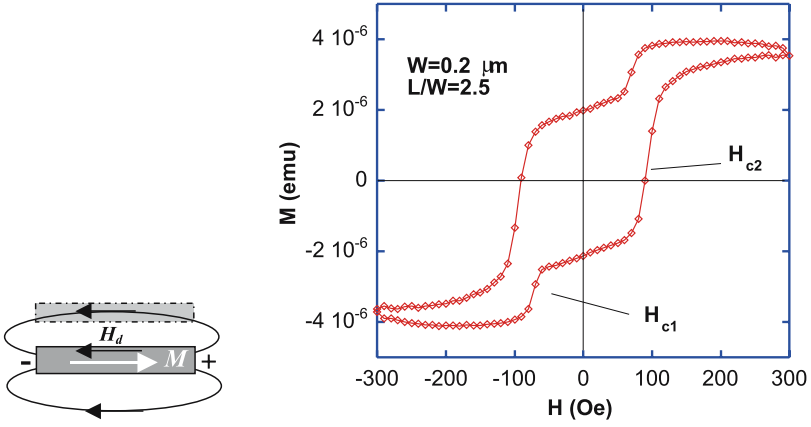
Fig. 7.33. Hysteresis loop of a patterned PSV element array (4 nm NiFeCo/4 nm Cu/6 nm NiFeCo). The remanent state is an anti-parallel state. When the field sweeps to the positive direction, the thin layer switches at a negative field
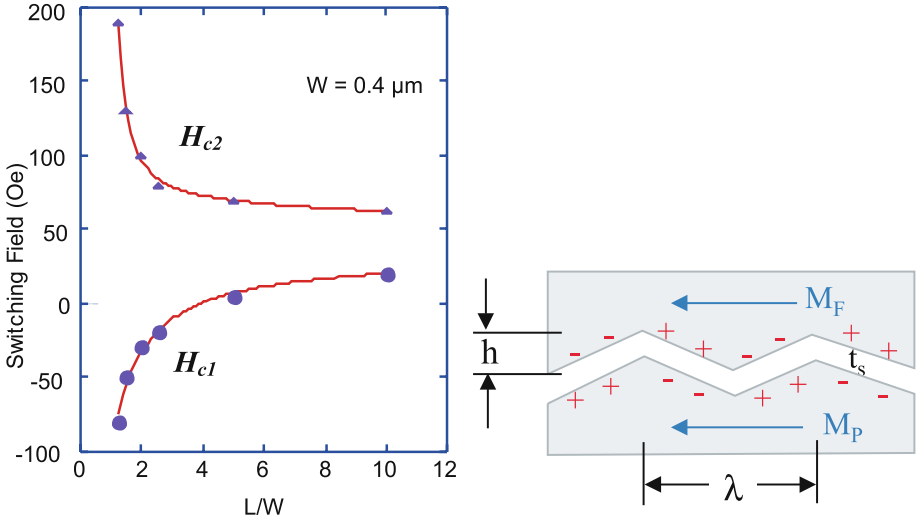

Fig. 7.34. Switching fields of two layers in 0.4 μm wide elements as a function of element aspect ratio. The thin layer switching field, H_{c1}, crosses zero at about $L/W = 4$

7.7.3 Inter-element Magnetostatic Interaction

At current DRAM density, each cell occupies $8F^2$, which means that the center-to-center separation is less than $3F$, and the nearest edge-to-edge separation is less than $2F$. As discussed in Sec. 7.3, the DRAM cell area factor also decreases in addition to the decrease in F itself. High-density MRAM demands a smaller cell size in future generations. This means that the inter-element distance will scale more rapidly
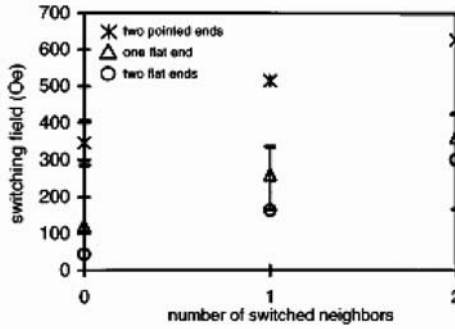
Fig. 7.35. Effect of switched neighbors on switching field of a chosen element in a linear chain of 26 nm thick, 200 nm wide and 3.5 μm long Co elements placed 50 nm (edge-to-edge) apart from each other. Different symbols represent different element shapes. As the neighboring elements switch, the demagnetizing field acting on the element pushes its switching field higher. This coupling field is quite strong (∼150 Oe) in this geometry (Data from [7.45])

than $2F$. A rough point-dipole estimation for a constant cell area factor suggests a $\mu/r^3 \propto F^2/F^3 = 1/F$ dependence of the inter-element coupling field strength. But the switching field itself also approximately follows $1/F$ (7.7). Therefore, the shrink in minimum feature size does not imply an increase in the inter-element coupling relative to the switching field. In practice, the inter-element coupling field also depends on the detailed shape and geometry of the elements as well as the inter-element spacing [7.51, 53, 64, 65]. However, more detailed micromagnetic analyses as well as systematic experiments are needed to further understand the effect of the coupling on both the switching field and switching mode in high-density MRAM.

7.7.4 Switching Field Distribution

Let us assume the distribution of the switching field in a 2D MRAM array is a Gaussian around the center $\langle H_c \rangle$ with a standard distribution σ. Upon the application of a half-select hard-axis field, $\langle H_c \rangle/2^{1.5}$, the Gaussian center shifts approximately to $\langle H_c \rangle/2^{1.5}$ according to the SW theory, if the starting distribution is narrow. (If the initial distribution is broad, the distribution is no longer a Gaussian when a hard-axis field is applied because of the non-linear nature of the SW astroid). In the meantime, the standard deviation is decreased by a factor of $2^{0.25}$. We can ignore this change in width. The two Gaussians must be separated from each other with a large enough distance to ensure that the bits are selectable. For example, if 6σ of the Gaussian distribution is selectable (10^{-6} error rate), the distribution should be so narrow that $6\sigma\langle(1-2^{-1.5})\rangle\langle H_c \rangle$, i.e. $2\sigma/\langle H_c \rangle < 0.2$. In submicron element arrays such as the one in Fig. 7.21, the switching astroid is far less steep than what the SW-model predicts, so the criterion for the switching distribution width must be more stringent.

In small magnetic elements approaching single-domain size, the magnetostatic energy is determined by the surface charges, $\sigma = \boldsymbol{M} \cdot \hat{\boldsymbol{n}}$, which varies with the surface

roughness. The shape variation can be a source of broad switching field distribution among 10^6–10^9 elements. In addition, inter-element magnetostatic coupling can be another important source of broad distribution in high density MRAM.

7.7.5 Thermal Stability

The anisotropy barrier, $K_u V$, decreases sharply due to the rapid shrink in minimum feature size. For recording media [7.66], a 10 year data retention time requires $K_u V/k_B T \sim 40$. This ratio is found to be about 100 for 10 nm-thick 200 nm $\times$ 1000 nm NiFe elements [7.67], and between 100 to 200 for 7.9 nm-thick 1 μm-wide NiFe elements [7.68]. In smaller and thinner elements, this ratio will further decrease. Moreover, in half-selected bits, according to the SW-model, the energy barrier decreases as $(H_c - H)^2$. At $H = H_c/2^{1.5}$, the energy barrier is decreased to $(1 - 2^{-1.5})^2 = 0.4$ of the original value. At any given time of writing, for a MRAM chip with total number of memory bits of N, $1/\sqrt{N}$ of the total memory bits are under this half-select condition. In addition, the thermally activated magnetization reversal is closely related to the dynamic switching with ultra-fast pulses [7.69]. This issue also needs further systematic investigation.

In summary, high-density MRAM offers a very attractive potential for high-performance memory devices. Further advances in MRAM development call for better understanding of magnetization reversal of patterned magnetic nanostructures. In general, as the size of the MRAM elements approaches the single-domain size, the switching mechanism appears to be simpler. However, in many product generations to come, micromagnetics will still play a role in magnetic switching of MRAM devices. In addition, even for single-domain devices, there are many challenging issues ahead that demand a further understanding of nanomagnetism.

References

7.1. B.D. Cullity, *Introduction to Magnetic Materials*, Addison-Wesley, 1972.

7.2. W. Renwick and A.J. Cole, *Digital Storage Systems*, Chapman & Hall Ltd, 1971.

7.3. B. Prince and G. Due-Gundersen, *Semiconductor Memories*, John Wiley & Sons Ltd. 1983.

7.4. B. Price, *Semiconductor Memories: A Handbook of Design, Manufacture, and Application* , Jonn Wiley & Sons Ltd., 1996.

7.5. J.F. Scott, *Ferroelectric Memories*, Springer-Verlag, 2000.

7.6. R.R. Katti and T. Zhu, *Attractive Magnetic Memories*, IEEE Circuits & Devices Magazine, **17**, 26 (2001).

7.7. S. Tehrani, Tunneling *Magnetoresistive Random Access Memory*, to appear in VLSI Symposium (June 2002).

7.8. S.A. Wolf, D.D. Awschalom, R.A. Buhrman, J.M. Daughton, S. von Molnár, M.L. Roukes, A.Y. Chtchelkanova, and D.M. Treger, *Spintronics: A Spin-Based Electronics Vision for the Future*, Science, **294**, 1488 (2001).

7.9. W. Reohr, H. Hönigschmid, R. Robertazzi, D. Gogl, F. Pesavento, S. Lammers, K. Lewis, C. Arndt, Y. Lu, H. Viehmann, R. Scheuerlein, L.-K. Wang, P. Trouilloud, S. Parkin, W. Gallagher, and G. Müller, *MTJ MRAM, A Magnetically Attractive RAM*, IEEE Circuits and Devices Magazine, July 2002 (to be published).

7.10. S. Chikazumi, *Physics of Ferromagnetism*, Clarendon Press (1997).

7.11. J. Kondo, *Anomalous Hall Effect and Magnetoresistance of Ferromagnetic Metals*, Progr. Theor. Phys. **27**, 772 (1962).

7.12. J.M. Daughton, *Magnetoresistive Memory Technology*, Thin Solid Films, **216**, 162 (1992).

7.13. A. Pohm, C. Comstock, and A. Hurst, *Quadrupled Non-Destructive Output from Memory Cells Using Reversed Word Fields*, J. Appl. Phys. **67**, 4881 (1990).

7.14. M.N. Baibich, J.M. Broto, A. Fert, F. Nguyen Van Dau, F. Petroff, P. Eitenne, G. Creuzet, A. Friederich, and J. Chazelas, *Giant Magnetoresistance of (100)Fe/(001)Cr Magnetic Superlattices*, Phys. Rev. Lett. **61**, 2472 (1988).

7.15. S.S.P. Parkin, Chapter 2.4, page 148, *Ultrathin Magnetic structures II*, ed. by B. Heinrich and J.A.C. Bland.

7.16. W.F. Egelhoff, Jr., P.J. Chen, C.J. Powell, M.D. Stiles, R.D. McMichael, C.-L. Lin, J.M. Siertsen, J.H. Judy, K. Takano, A.E. Berkowitz, T.C. Anthony, and J.A. Brug, *Optimizing the Giant Magnetoresistance of Symmetric and Bottom Spin-Valves*, J. Appl. Phys. **79**, 5277 (1996).

7.17. D.D. Tang, P.K. Wang, V.S. Speriosu, S. Le, R.E. Fontana, and S. Rishton, *An IC Process Compatible Nonvolatile Magnetic RAM*, IEDM Tech. Digest. New York: IEEE, 1995, pp. 997–1000.

7.18. S. Tehrani, E. Chen, M. Durlam, T. Zhu, and H. Goronkin, *High Density Nonvolatile Magnetoresistive RAM*, IEDM Tech. Digest, 193 (1996).

7.19. S. Tehrani, J.M. Slaughter, E. Chen, M. Durlam, J. Shi, and M. DeHerrera, *Progress and Outlook for MRAM Technology*, IEEE Trans. Magn. **35**, 2814 (1999).

7.20. S. Tehrani, E. Chen, M. Durlam, M. DeHerrera, J.M. Slaughter, J. Shi, and G. Kerszykowski, *High Density Submicron Magnetoresistive Random Access Memory*, J. Appl. Phys. **85**, 5822 (1999).

7.21. J.M. Daughton, *Magnetic Tunneling Applied to Memory*, J. Appl. Phys. **81**, 3758 (1997).

7.22. T. Miyazaki and N. Tezuka, *Giant Magnetic Tunneling Effect in Fe/Al$_2$O$_3$/Fe Junction*, J. Magn. Magn. Mater. **139**, L231 (1995).

7.23. R.C. Sousa, J.J. Sun, V. Soares, P.P. Frestaa, A. Kling, M.F. da Silva, and J.C. Soares, *Large Tunneling Magnetoresistance Enhancement by Thermal Annel*, Appl. Rev. Lett. **73**, 3288 (1998).

7.24. J.S. Moodera, L.R. Kinder, T.M. Wong, and R. Meservey, *Large Magnetoresistance at Room Temperature in Ferromagnetic Thin Film Tunnel Junctions*, Phys. Rev. Lett. **74**, 3272 (1995).

7.25. W.J. Gallagher, S.S.P. Parkin, Y. Lu, X.P. Bian, A. Marley, R.A. Altman, S.A. Rishton, K.P. Roche, C. Jahnes, T.M. Shaw, and G. Xiao, *Microstructured Magnetic Tunnel Junctions*, J. Appl. Phys. **81**, 3741 (1997).

7.26. J.G. Simmons, *Generalized Formula for the Electric Tunnel Effect between Similar Electrodes Separated by a Thin Insulating Film*, J. Appl. Phys. **34**, 1793 (1963).

7.27. M. Julliere, *Tunneling between Ferromagnetic Films*, Phys. Lett. **54A**, 225 (1975).

7.28. S. Tehrani, B. Engel, J.M. Slaughter, E. Chen, M. DeHerrera, M. Durlam, P. Naji, R. Whig, J. Janesky, and J. Calder, *Recent Development in Magnetic Tunnel Junction MRAM*, IEEE Trans. Magn. **36**, 2752 (2000).

7.29. J.-G. Zhu, Y.F. Zheng, and G.A. Prinz, *Ultrahigh Density Vertical Magnetoresistive Random Access Memory*, J. Appl. Phys. **87**, 6668 (2000).

7.30. M. Johnson, B. Bennett, and M. Yang, *Hybrid Ferromagnetic Semiconductor Nonvolatile Memory*, IEEE Trans. Magn. **34**, 1054 (1998).

7.31. B. Heinrich, *Magnetic Nanostructures: from Physical Principles to Spintronics*, Canadian J. Phys. **78**, 161 (2000).

7.32. Available on ITRS website: http://public.itrs.net/Files/2001ITRS/Home.htm.

7.33. A.H. Eschenfelder, *Magnetic Bubble Technology*, Springer-Verlag, 1981.

7.34. C. Kittel, *Physical Theory of Ferromagnetic Domains,* Rev. Mod. Phys. **21**, 541 (1949).

7.35. A. Hubert and R. Schäfer, *Magnetic Domains,* Springer-Verlag, 2000.

7.36. E.C. Stoner and E.P. Wohlfarth, *A Mechanism of Magnetic Hysteresis in Heterogeneous Alloys*, Phil. Trans. Roy. Soc. A**240**, 599 (1948).

7.37. M. Lederman, S. Schultz, and M. Ozaki, *Measurement of the Dynamics of the Magnetization Reversal in Individual Single-Domain Ferromagnetic Particles*, Phys. Rev. Lett. **73**, 1986 (1994).

7.38. W. Wernsdofer, B. Doudin, D. Mailly, K. Hasselbach, A. Benoit, J. Meier, J.-Ph. Ansermet, and B. Barbara, *Nucleation of Magnetization Reversal in Individual Nanosized Nickel Wires*, Phys. Rev. Lett. **77**, 1873 (1996).

7.39. For example, A.H. Morrish, *The Physical Principles of Magnetism, IEEE Press, 2001.*

7.40. J.A. Osborn, *Demagnetizing Factors of the General Ellipsoid*, Phys. Rev. **67**, 351 (1945).

7.41. J.C. Slonczewski, *Theory of Magnetic Hysteresis in Films and Its Application to Computers,* Research Report RM 003.111.224 (IBM Corp., 1956).

7.42. J. Shi, T. Zhu, M. Durlam, E. Chen, S. Tehrani, Y.F. Zheng, and J.-G. Zhu, *End Domain States and Magnetization Reversal in Submicron Magnetic Structures*, IEEE Trans. Magn. 34, 997 (1998).

7.43. R.P. Cowburn, *Property Variation with Shape in Magnetic Nanoelements*, J. Phys. D, **33**, R1 (2000).

7.44. W.F. Brown, Jr., *Micromagnetics*, Wiley, 1963.

7.45. A. Aharoni, *Introduction to the Theory of Ferromagnetism*, Clarenton Press, 1996.

7.46. J. Shi and S. Tehrani, *Edge-Pinned States in Patterned Submicron NiFeCo Structures*, Appl. Phys. Lett. **77**, 1692 (2000).

7.47. K.J. Kirk, M.R. Scheinfein, J.N. Chapman, S. McVitie, M.F. Gillies, B.R. Ward and J.G. Tennant, *Role of Vortices in Magnetization Reversal of RectangularElements*, J. Phys. D., **34**, 160 (2001).

7.48. J. Shi, S. Tehrani, M.R. Scheinfein, *Geometry Dependence of Magnetization Vortices in Patterned Magnetic Elements*, Appl. Phys. Lett. **76**, 2588 (2000).

7.49. J. Shi, T. Zhu, S. Tehrani, Y.F. Zheng and J.-G. Zhu, *Switching Anomaly and Magnetization Vortices of 200 A Thick NiFeCo Elements in One-Micron Patterned Arrays,* J. Magn. Magn. Mat. **198–199**, 251 (1999).

7.50. J. Shi, S. Tehrani, T. Zhu, Y.F. Zheng and J.-G. Zhu, *Magnetization Vortices and Anomalous Switching in Patterned Submicron Structures*, Appl. Phys. Lett. **74**, 2525 (1999).

7.51. K.J. Kirk, J.N. Chapman, and C.D.W. Wilkinson, *Switching Fields and Magnetostatic Interactions of Thin Film Magnetic Nanoelements*, Appl. Phys. Lett. **71**, 539 (1997).

7.52. R.P. Cowburn, D.K. Koltsov, A.O. Adeyeye, M.E. Welland, D.M. Tricker, *Single-Domain Circular Nanomagnets*, Phys. Rev. Lett. **83**, 1042 (1999).

7.53. R.E. Dddunin-Borkowski, M.R. MaCartney, B. Kardynal, D.J. Smith, M.R. Scheinfein, *Switching Asymmetries in Closely Coupled Magnetic Nanostructure Arrays,* Appl. Phys. Lett.**75**, 2641(1999).

7.54. E. Girgis, J. Schelten, J. Shi, J. Janesky, S. Tehrani, and H. Goronkin, *Switching Characteristics and Magnetization Vortices of Thin-Film Cobalt in Nanometer-Scale Patterned Arrays,* Appl. Phys. Lett. **76**, 3780 (2000).

7.55. T. Shinjo, T. Okuno, R. Hassdorf, K. Shigeto, and T. Ono, *Magnetic Vortex Core Observation in Circular Dots of Permalloy*, Science, **289**, 930 (2000).

7.56. LLG Micromagnetics Simulator is a commercial micromagnetic program. http://llgmicro.home.mindspring.com/.

7.57. A.F. Popkov, L.L. Savchenko, N.V. Vorotnikova, S. Tehrani, and J. Shi, *Edge Pinning Effect in Single- and Three-Layer Patterns*, Appl. Phys. Lett. **77**, 277 (2000).

7.58. T.-N. Fang and J.-G. Zhu, *Switching Fluctuations and Density Limitation of Pseudospin Valve Memory*, J. Appl. Phys. 87, 7061(2000).

7.59. J. Shi, T. Zhu, S. Tehrani, *MRAM with Aligned Magnetic Vectors,* U.S. Patent No. 5,757,695 (1997).

7.60. A. Arrott (private communication).

7.61. T. Zhu, J. Shi, S. Tehrani, M. Durlam and E. Chen, *Switching Characteristics of Submicron Dimension Permalloy Sandwich Films*, IEEE Trans. Magn. **33**, 3601 (1997).

7.62. J. Zhang and R.M. White, *Topological Coupling in Spin Valve Type Mulitlayers*, IEEE Trans. Mang. **32**, 4630 (1996).

7.63. J.M. Slaughter (private communication).

7.64. J. Janesky, N.D. Rizzo, L. Savtchenko, B. Engel, J.M. Slaughter, and S. Tehrani, *Magnetostatic Interactions between Sub-Micrometer Patterned Magnetic Elements,* IEEE Trans. Magn. **37**, 2052 (2001).

7.65. M.C. Abraham, H. Schmidt, T.A. Savas, H.I. Smith, C.A. Ross, and R.J. Ram, *Magnetic Properties and Interactions of Single-Domain Nanomagnets in a Periodic Array*, J. Appl. Phys. 89, 5667 (2001).

7.66. D. Weller and A. Moser, *Thermal Effect Limits in Ultrahigh-Density Magnetic Recording*, IEEE Trans. Magn. 35, 4423 (1999).

7.67. J. Li and S. Tehrani and J. Shi, *Temperature-Dependent Switching Properties in Patterned 200nm NiFe Structures*, Appl. Phys. Lett. **79**, 3821 (2001).

7.68. H.Q. Yin and W.D. Doyle, *Thermal Relaxation of Soft Magnetic Patterned Elements*, to appear in J. Appl. Phys. (2002).

7.69. R.H. Koch, G. Grinstein, G.A. Keefe, Yu Lu, P.L. Trouilloud, W.J. Gallagher, and S.S.P. Parkin, *Thermally Assisted Magnetization Reversal in Submicron-Sized Magnetic Thin Films,* Phys. Rev. Lett. 84, 5419 (2000).